Cell Reports
Physical Science

CellPress
OPEN ACCESS

Article

Regulating C_2H_2/CO_2 adsorption selectivity by electronic-state manipulation of iron in metal-organic frameworks

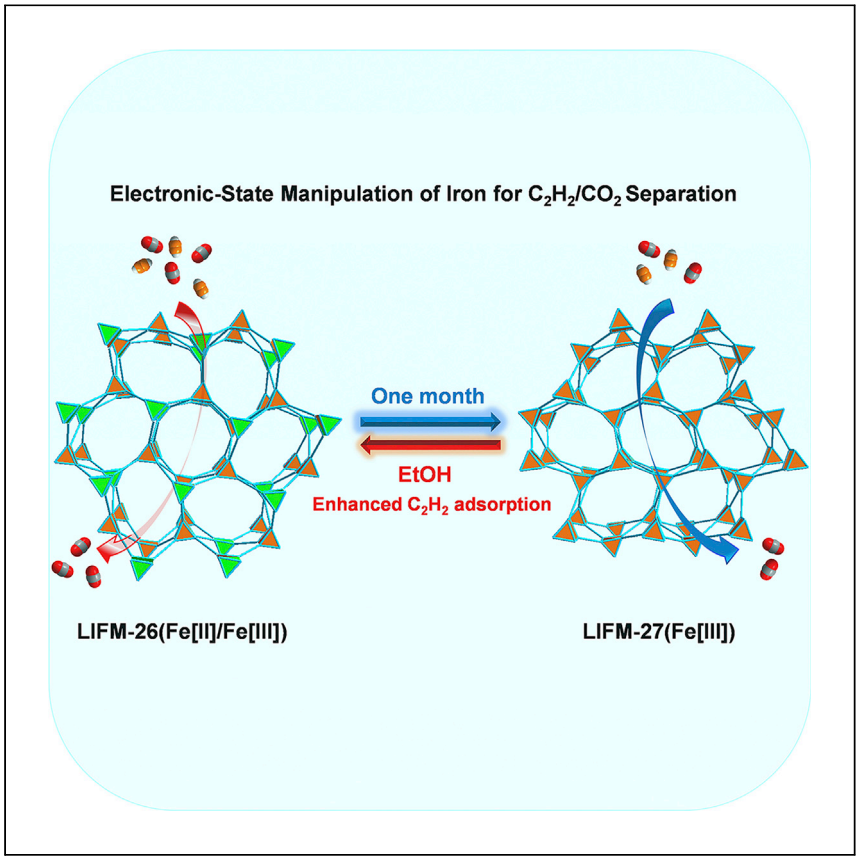

Chen et al. report a metal electronic-state manipulation strategy to construct a pair of isostructural and interconvertible Fe-MOFs featuring open Fe centers with different electron densities for efficient C_2H_2/CO_2 separation. They show that the presence of Fe[II] centers with a medium-spin-state trail plays a crucial role in the enhanced C_2H_2 selective adsorption.

Cheng-Xia Chen, Tony Pham, Kui Tan, ..., Lei Zhang, Cheng-Yong Su, Shengqian Ma

cesscy@mail.sysu.edu.cn (C.-Y.S.)
Shengqian.Ma@unt.edu (S.M.)

Highlights

The electronic state of Fe can be purposely tuned to regulate C_2H_2/CO_2 separation

Increasing electron density of Fe centers results in enhanced C_2H_2 adsorption

The interconvertible nature deepens understanding of structure-property relationship

Distinct adsorption mechanism is unveiled through *in situ* FTIR and molecular simulation

Chen et al., Cell Reports Physical Science 3, 100977
August 17, 2022
https://doi.org/10.1016/j.xcrp.2022.100977

Please cite this article in press as: Chen et al., Regulating C_2H_2/CO_2 adsorption selectivity by electronic-state manipulation of iron in metal-organic frameworks, Cell Reports Physical Science (2022), https://doi.org/10.1016/j.xcrp.2022.100977

Cell Reports
Physical Science

Article

Regulating C_2H_2/CO_2 adsorption selectivity by electronic-state manipulation of iron in metal-organic frameworks

Cheng-Xia Chen,[1,2] Tony Pham,[3] Kui Tan,[4] Rajamani Krishna,[6] Pui Ching Lan,[2] Longfei Wang,[1] Songbo Chen,[7] Abdullah M. Al-Enizi,[8] Ayman Nafady,[8] Katherine A. Forrest,[3] Haiping Wang,[2] Sicheng Wang,[2] Chuan Shan,[3] Lei Zhang,[5] Cheng-Yong Su,[1,9,*] and Shengqian Ma[2,9,*]

SUMMARY

The separation of C_2H_2 from C_2H_2/CO_2 mixture is of great importance, yet highly challenging in the petrochemical industry due to their similar physicochemical properties. While open-metal sites (OMSs) in metal-organic frameworks (MOFs) are known to possess high affinity toward C_2H_2, its selective adsorption performance regulated by the electronic state of the same OMSs remains unexplored. Here, we report a metal electronic-state manipulation approach to construct a pair of isostructural Fe-MOFs, namely LIFM-26(Fe[II]/Fe[III]) and LIFM-27(Fe[III]) with different Fe[II] or Fe[III] oxidation states on the Fe centers, which display mixed-valent Fe[II]/Fe[III] centers in the former and sole Fe[III] centers in the latter. Remarkably, LIFM-26(Fe[II]/Fe[III]) shows significantly enhanced C_2H_2 uptake capacity than LIFM-27(Fe[III]), attested by adsorption isotherms and IAST calculations, as well as simulated and experimental breakthrough experiments. Furthermore, *in situ* infrared (IR) and molecular calculations unveil that the presence of Fe[II] in LIFM-26(Fe[II]/Fe[III]) results in stronger Fe[II]–C_2H_2 interactions than Fe[III]–C_2H_2, which plays a key role in the C_2H_2/CO_2 separation.

INTRODUCTION

Industrial chemical separations account for 10%–15% of the global energy consumption, which corresponds to half of the United States's industrial energy use.[1] Among them, acetylene (C_2H_2) purification represents an energy- and cost-intensive process.[2] As one of the most widely used feedstocks in the petroleum industry, C_2H_2 is mainly produced by the combustion of methane or thermal cracking of petroleum, with CO_2 as the major byproduct.[3] Therefore, separating CO_2 from C_2H_2/CO_2 gas mixture is of great importance. Presently, the industrial separation of CO_2 from C_2H_2 is usually implemented through solvent extraction and cryogenic distillation, leading to intensive costs and energy penalties due to their similar physicochemical properties (molecular sizes and shapes: 3.32 × 3.34 × 5.70 $Å^3$ for C_2H_2, 3.18 × 3.33 × 5.36 $Å^3$ for CO_2; boiling points: 189.3 and 194.7 K for C_2H_2 and CO_2, respectively).[4,5] As a result, adsorptive separation based on porous solid materials has drawn much attention owing to the advantage of dramatically reducing the energy and cost consumption.[6–10]

Owing to their structural diversity, designable pore size, high pore volume, and tunable functionalities, metal-organic frameworks (MOFs) have shown great

[1]MOE Laboratory of Bioinorganic and Synthetic Chemistry, Lehn Institute of Functional Materials, School of Chemistry, Sun Yat-Sen University, Guangzhou 510275, China

[2]Department of Chemistry, University of North Texas, Denton, TX 76201, USA

[3]Department of Chemistry, University of South Florida, Tampa, FL 33620, USA

[4]Department of Materials Science & Engineering, University of Texas at Dallas, Richardson, TX 75080, USA

[5]College of Materials Science and Engineering, Fujian University of Technology, Fuzhou 350118, China

[6]Van't Hoff Institute for Molecular Sciences, University of Amsterdam, 1098 Amsterdam, the Netherlands

[7]School of Physical Science and Technology, Lanzhou University, Lanzhou 730000, China

[8]Department of Chemistry, College of Science, King Saud University, Riyadh 11451, Saudi Arabia

[9]Lead contact

*Correspondence: cesscy@mail.sysu.edu.cn (C.-Y.S.), Shengqian.Ma@unt.edu (S.M.)

https://doi.org/10.1016/j.xcrp.2022.100977

Please cite this article in press as: Chen et al., Regulating C_2H_2/CO_2 adsorption selectivity by electronic-state manipulation of iron in metal-organic frameworks, Cell Reports Physical Science (2022), https://doi.org/10.1016/j.xcrp.2022.100977

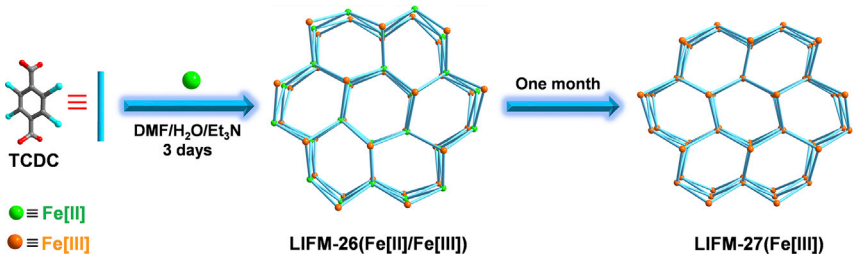

Scheme 1. Schematic synthetic route of Fe-MOF isostructures with different ratios of Fe[II] and Fe[III] centers through a metal electronic-state manipulation strategy

potentials in gas adsorption and separation involving C_2H_2/CO_2, C_2H_4/C_2H_6, C_3H_6/C_3H_8, N_2/O_2, CO/H_2, and CO/N_2.[8–15] However, it is still challenging to rationally design MOFs for C_2H_2/CO_2 separation due to their similar dynamic sizes and volatility. Tremendous efforts have been devoted to developing highly effective MOF adsorbents, suggesting that the introduction of open-metal sites (OMSs) into suitable pore space is most likely to be competent for this task.[16–24] The suitable pore space (appropriate pore size, high pore volume, and polar pore surface) can render the framework with a high C_2H_2 adsorption working capacity and facilitates adsorption dynamics.[25–30] In addition, the OMSs with exposed partial positive charges not only behave as Lewis-acid-accepting electrons from the electron lone pair orbital of C_2H_2 but also function as a π-bond back donor providing electrons to C_2H_2 (delocalizing d electrons to the antibonding π^* orbitals of C_2H_2), thus resulting in preferential adsorption toward C_2H_2 over CO_2.[26,31–33] However, it is extremely difficult to combine exposed positive charges and strong π back donors into a single material. Actually, most MOFs with OMSs present weak π-bond back donation due to their electron-poor metal centers, and only a few MOFs featuring exposed electron-rich metal centers are found to be suitable for π-bond back donation.[32,34–36]

In order to functionalize MOFs with electron-rich OMSs for highly selective C_2H_2 adsorption, it is anticipated that the manipulation of the mixed-valent electronic states of exposed metal centers in a suitable MOF pore space is an effective yet challenging strategy. The introduction of an appropriate low-valent metal center can impart enhanced π back donation, thereby facilitating the preferential C_2H_2 adsorption over CO_2, while the presence of a high-valent metal center can allow for facile desorption of C_2H_2 due to the moderate metal-adsorbate interactions. Herein, we report a pair of isostructural Fe-MOFs, namely LIFM-26(Fe[II]/Fe[III])[37] and LIFM-27(Fe[III]) (LIFM stands for Lehn Institute of Functional Materials) that possess pore spaces constructed from the same perchlorinated ligand (2,3,5,6-tetrachloride terephthalic acid [TCDC]) (Scheme S1) and oxidation-state variant Fe[II]/Fe[III] centers (Scheme 1). Both structures feature coordinately unsaturated Fe centers, in which the ratios of Fe[II] and Fe[III] can be purposely tuned through an *in situ* redox process (Scheme 1), endowing the isostructural Fe-MOFs with distinct C_2H_2 selective adsorption performance. It is worth noting that LIFM-26(Fe[II]/Fe[III]) and LIFM-27(Fe[III]) are interconvertible as the isostructures of $(Fe[II]/Fe[III])_3O(TFBDC)_3$ (TFBDC = 2,3,5,6-tetrafluorobenzene-1,4-dicarboxylate),[38] providing ideal examples for studying the inherent relationship between the metal electronic-state and adsorption performance. Compared with LIFM-27(Fe[III]), the increased electron density in LIFM-26(Fe[II]/Fe[III]) affords much higher C_2H_2 uptake capacity and superior C_2H_2 selectivity over CO_2 in the low-pressure region, due to the stronger Fe[II]-adsorbate interactions than Fe[III]-C_2H_2, which illustrates that manipulation of the electronic-state of OMSs can lead to enhanced preferential C_2H_2 adsorption.

Please cite this article in press as: Chen et al., Regulating C_2H_2/CO_2 adsorption selectivity by electronic-state manipulation of iron in metal-organic frameworks, Cell Reports Physical Science (2022), https://doi.org/10.1016/j.xcrp.2022.100977

Moreover, the combined studies of ideal adsorbed solution theory (IAST) calculations, simulated/experimental dynamic breakthrough experiments, molecular simulations, and *in situ* infrared (IR) analysis well confirm that the exposed Fe[II] center with a strong π back-donation character plays a crucial role in the enhanced C_2H_2/CO_2 separation.

RESULTS AND DISCUSSION

Synthesis and structure determination

LIFM-26(Fe[II]/Fe[III]) was synthesized according to our previously reported method with a slight modification.[37] The slow diffusion of triethylamine vapor into a mixture of *N*,*N*′-dimethylformamide (DMF) and water dissolving TCDC ligand and $FeCl_2$ for 3 days afforded LIFM-26(Fe[II]/Fe[III]) crystals, during which Fe[II] was partially oxidized into Fe[III]. In comparison, LIFM-27(Fe[III]) was obtained by extending the vapor diffusion time to 1 month, during which Fe[II] was completely oxidized into Fe[III] (Scheme 1). Notably, LIFM-27(Fe[III]) can be transformed back to LIFM-26(Fe[II]/Fe[III]) via soaking the samples in ethanol solution for 3 days at 75°C (denoted as LIFM-27(Fe[III])-EtOH; Figure S10), showing solvent-dependent redox property. Single-crystal X-ray diffraction (SCXRD) analyses reveal that LIFM-26(Fe[II]/Fe[III]) and LIFM-27(Fe[III]) crystalize in the *P*-3 and *P*21/n space groups, respectively (Table S1). Both of them possess the same acs net topology as $(Fe[II]/Fe[III])_3O(TFBDC)_3$, which is constructed from perfluorinated ligand TFBDC and $FeCl_2$ (Figure 1). Compared with $(Fe[II]/Fe[III])_3O(TFBDC)_3$, the Fe_3O clusters in LIFM-26(Fe[II]/Fe[III]) and LIFM-27(Fe[III]) are twisted without the C_3 axis of symmetry perpendicular to the Fe_3O plane due to the large steric hindrance of chlorine atoms. The Fe-(μ_3-O)-Fe angles in LIFM-26(Fe[II]/Fe[III]) are 115.8°, 120.9°, and 123.3°, while those in LIFM-27(Fe[III]) are 118.4°, 118.8°, and 122.8°. In these three structures, every Fe_3O cluster connects six ligands, whereas every ligand links two independent Fe_3O clusters, thus forming a three-dimensional (3D) framework containing 1D channels (Figures 1C–1E). Notably, $(Fe[II]/Fe[III])_3O(TFBDC)_3$ presents one type of round channel along the c axis with an aperture size of ca. 13.2 Å (Figures 1C and 1F), while LIFM-26(Fe[II]/Fe[III]) features two types of different channels functionalized by chlorine atoms along the c axis, i.e., one round channel with an aperture size of ca. 9.0 Å and one elliptic channel with a pore size of ca. 8.2 × 11.5 $Å^2$ (Figures 1D, 1G, and S1). As for LIFM-27(Fe[III]), there is one type of elliptic channel decorated by chlorine atoms along the c axis with a pore size of about 7.5 × 9.7 $Å^2$ (Figures 1E, 1H, and S2). Additionally, all three frameworks present one type of tetrahedral cage (diameter ca. 7.0 Å) constructed from six ligands and five Fe_3O clusters (Figure 1I).

In order to probe the oxidation and spin states of Fe centers, ^{57}Fe Mössbauer spectroscopic experiments were carried out for LIFM-26(Fe[II]/Fe[III]), LIFM-27(Fe[III]), and LIFM-27(Fe[III])-EtOH (Figures 2 and S3–S5; Table S2). The spectra of LIFM-26(Fe[II]/Fe[III]) can be fitted by one type of doublet and one type of singlet, revealing two kinds of Fe species with adsorption area ratios of 47.65% and 52.35%, corresponding to the amounts of Fe[II] and Fe[III] centers (0.9:1.0) (Figure 2A, D1 line). For comparison, only one type of fitting doublet in LIFM-27(Fe[III]) was observed, confirming the existence of sole Fe[III] species (Figure 2B). LIFM-27(Fe[III])-EtOH also shows two kinds of Fe species similar to LIFM-26(Fe[II]/Fe[III]) yet with different adsorption area ratios, implying a variation of Fe[II] and Fe[III] species (Fe[II]:Fe[III] = 0.5:1.0; Figure S5). As shown in Figure 2A, the D2 line can readily be assigned to high-spin Fe[III] species in LIFM-26(Fe[II]/Fe[III]) with isomer shift δ = 0.78 mm/s,[34] while the D3 line can be assigned to medium-spin Fe[II] species with isomer shift δ = 0.31 mm/s and quadrupole splitting value

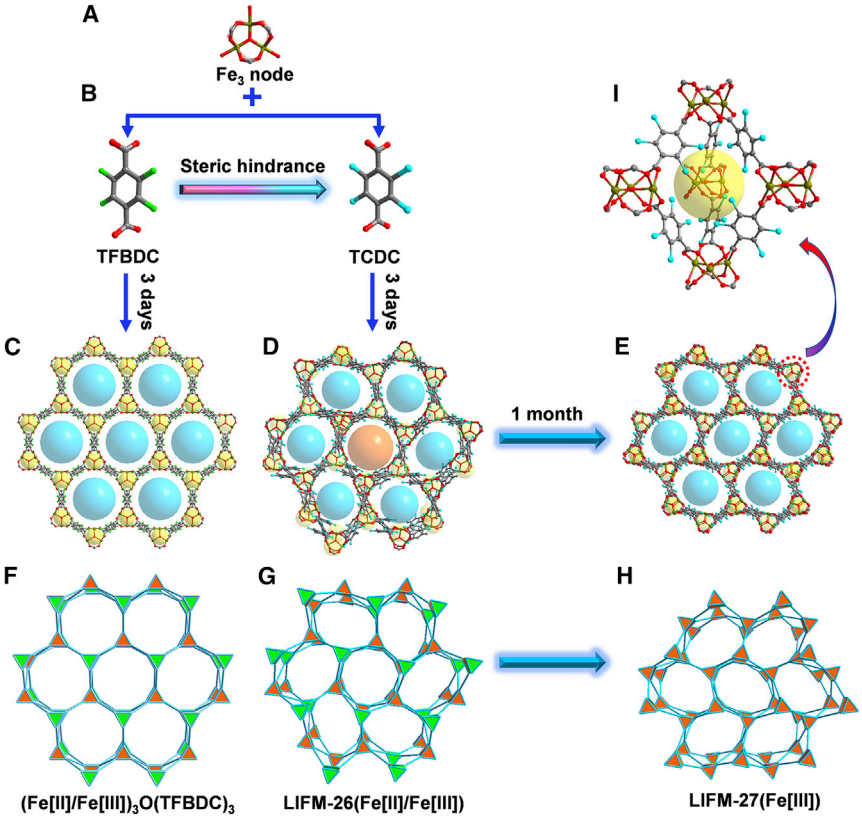

Figure 1. The schematic construction route of the 3D-MOFs

(A) Trimeric Fe_3O cluster.

(B) TFBDC and TCDC ligands.

(C–E) The 3D structures of (C) $(Fe[II]/Fe[III])_3O(TFBDC)_3$, (D) LIFM-26(Fe[II]/Fe[III]), and (E) LIFM-27(Fe[III]).

(F–H) The corresponding network topologies of (F) $(Fe[II]/Fe[III])_3O(TFBDC)_3$, (G) LIFM-26(Fe[II]/Fe[III]), and (H) LIFM-27(Fe[III]).

(I) The tetrahedral cage in three isostructural MOFs.

ΔE_Q = 0.56 mm/s,[34] suggesting the existence of a strong π back donation in LIFM-26(Fe[II]/Fe[III]). For LIFM-27(Fe[III]), the Mössbauer spectra reveal only one type of high-spin Fe[III] species with isomer shift δ = 0.44 mm/s.

Purity and porosity

Powder X-ray diffraction (PXRD) patterns were conducted to confirm the phase purity of the as-synthesized samples (Figures S8, S9, and S11), and the scanning electron microscope (SEM) images unveil similar crystal morphology (Figure S7). Thermal gravimetric analyses (TGAs) indicate comparable thermal stability of two isostructural MOFs up to 250°C (Figure S6). In contrast to $(Fe[II]/Fe[III])_3O(TFBDC)_3$ (Figure S11), both LIFM-26(Fe[II]/Fe[III]) and LIFM-27(Fe[III]) retain good crystallinity after activation under high vacuum, indicative of their good framework robustness (Figures S8 and S9). N_2 sorption isotherms at 77 K were collected to evaluate the permanent porosity of all three samples. As shown in Figure 3A, LIFM-26(Fe[II]/Fe[III]) (356 $cm^3\ g^{-1}$) and LIFM-27(Fe[III]) (310 $cm^3\ g^{-1}$) show much higher N_2 uptakes than $(Fe[II]/Fe[III])_3O(TFBDC)_3$ (17 $cm^3\ g^{-1}$) due to loss of its crystallinity after activation (Figure S11). Both LIFM-26(Fe[II]/Fe[III]) and LIFM-27(Fe[III]) show typical type I adsorption isotherms with the Brunauer-Emmett-Teller (BET) surface areas of 1,403 and 1,174 $m^2\ g^{-1}$, respectively, and the total pore volumes are 0.55 and 0.48 $cm^3\ g^{-1}$, respectively (Figures S12–S14; Table S3). The pore sizes of

Please cite this article in press as: Chen et al., Regulating C_2H_2/CO_2 adsorption selectivity by electronic-state manipulation of iron in metal-organic frameworks, Cell Reports Physical Science (2022), https://doi.org/10.1016/j.xcrp.2022.100977

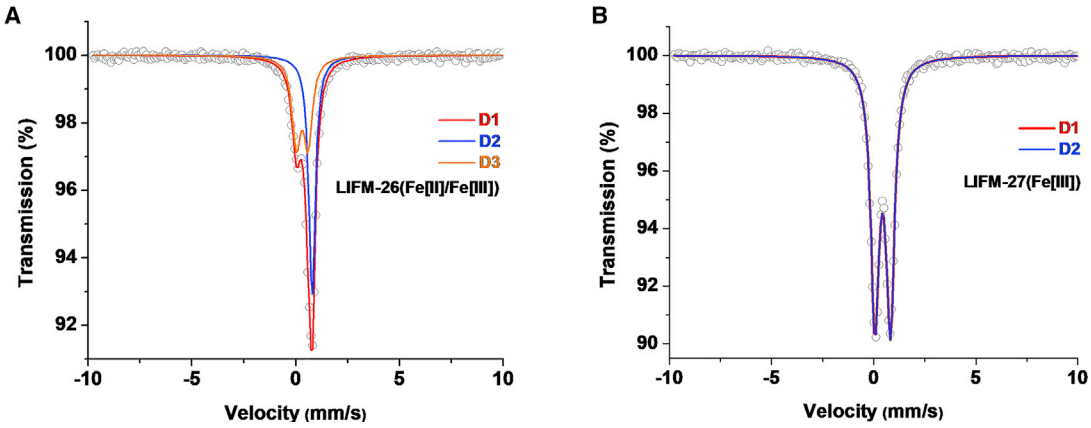

Figure 2. The ^{57}Fe Mössbauer Spectroscopy collected at 298 K

(A) LIFM-26(Fe[II]/Fe[III]).

(B) LIFM-27(Fe[III]).

LIFM-26(Fe[II]/Fe[III]) are calculated to be 6.8, 8.0, and 10.1 Å by density functional theory (DFT) analysis, while those of LIFM-27(Fe[III]) are 6.8 and 8.0 Å (Figure S15), matching well with the corresponding structural analyses. Additionally, we also evaluated the porosity of LIFM-27(Fe[III])-EtOH, which exhibits the BET surface area and pore volumes of 1,330 $m^2\ g^{-1}$ and 0.53 $cm^3\ g^{-1}$, falling between those of LIFM-26(Fe[II]/Fe[III]) and LIFM-27(Fe[III]) (Figure S16; Table S4).

Adsorption studies

The suitable pore structures of two isostructural Fe-MOFs as described above, including appropriate pore size and high pore volume as well as polar pore surface, are anticipated to facilitate C_2H_2 adsorption. To examine the effectiveness of the variant electronic state of OMSs on the adsorption performance, we selected C_2H_2 as a model gas molecule for evaluation. The C_2H_2 adsorption isotherms of both MOFs were measured at 273, 285, and 298 K, respectively (Figures 3B, 3C, S17, S19–S21, and S23–S24). Evidently, LIFM-26(Fe[II]/Fe[III]) showed much higher C_2H_2 uptake capacity (181 and 131 $cm^3\ g^{-1}$ at 273 and 298 K, 1 bar, respectively) than LIFM-27(Fe[III]) (128 and 97 $cm^3\ g^{-1}$ at 273 and 298 K, 1 bar, respectively), suggesting that Fe[II] center with higher electron density for stronger π back donation in LIFM-26(Fe[II]/Fe[III]) can effectively improve its adsorption behavior. Specifically, LIFM-26(Fe[II]/Fe[III]) (17.0 $cm^3\ g^{-1}$) can take up more than four times of C_2H_2 than LIFM-27(Fe[III]) (4.2 $cm^3\ g^{-1}$) at low pressure (3.4 mbar) (Figure 3D). Moreover, the C_2H_2 uptake capacity of LIFM-26(Fe[II]/Fe[III]) is much higher than that of $(Fe[II]/Fe[III])_3O(TFBDC)_3$ (Figures 3B and S25), and is also higher than many other known MOFs like Zn-MOF-74 (122 $cm^3\ g^{-1}$),[31] UTSA-74a (104 $cm^3\ g^{-1}$),[33] and PCP-33 (122 $cm^3\ g^{-1}$),[39] but is lower than some MOFs like FJI-H8-R series (174–229 $cm^3\ g^{-1}$),[17,24] MIL-160 (191 $cm^3\ g^{-1}$),[40] SIFSIX-Cu-TPA (185 $cm^3\ g^{-1}$),[41] and FJU-90a (180 $cm^3\ g^{-1}$) (Table S5).[42] To further confirm the effect of low-valent Fe(II) center, the C_2H_2 adsorption of LIFM-27(Fe[III])-EtOH, in which the amount of Fe[II] center is less than the prototypical LIFM-26(Fe[II]/Fe[III]), was measured at 298 K. As expected, the C_2H_2 uptake by LIFM-27(Fe[III])-EtOH was lower than LIFM-26(Fe[II]/Fe[III]) but higher than LIFM-27(Fe[III]) (Figures S30–S32). Additionally, the CO_2 adsorption isotherms were performed on both Fe-MOFs. LIFM-26(Fe[II]/Fe[III]) can take up 80 $cm^3\ g^{-1}$ CO_2 at 298 K and 1 bar, while the uptake capacity of LIFM-27(Fe[III]) is 51 $cm^3\ g^{-1}$ under the same condition (Figures 3B, 3C, S18, and S22). These

Please cite this article in press as: Chen et al., Regulating C_2H_2/CO_2 adsorption selectivity by electronic-state manipulation of iron in metal-organic frameworks, Cell Reports Physical Science (2022), https://doi.org/10.1016/j.xcrp.2022.100977

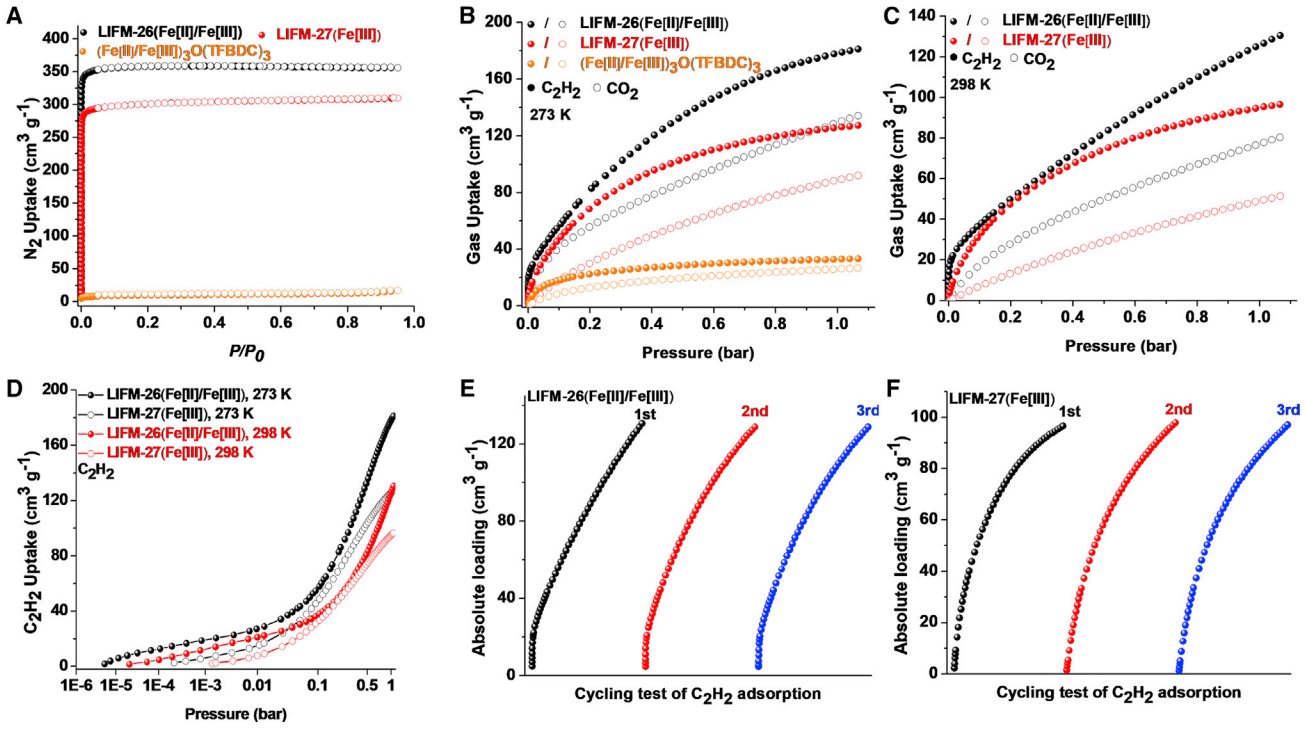

Figure 3. Gas adsorption properties of the three MOFs

(A) The N_2 adsorption of all the three MOFs at 77 K.

(B and C) The C_2H_2 and CO_2 adsorption isotherms at (B) 273 and (C) 298 K.

(D) The C_2H_2 adsorption isotherms.

(E and F) The repetitive C_2H_2 adsorption isotherms of (E) LIFM-26(Fe[II]/Fe[III]) and (F) LIFM-27(Fe[III]).

results indicate that the gas adsorption performance of the two isostructural Fe-MOFs can be finely tuned by regulating the electron state of OMSs. Furthermore, the continuous C_2H_2 and CO_2 adsorption isotherms on both Fe-MOFs were carefully performed, verifying their excellent reusability (Figures 3E, 3F, and S26–S29).

The isosteric heat (Q_{st}) of C_2H_2 and CO_2 on both MOFs were calculated using the Clausius-Clapeyron equation based on their adsorption isotherms at three different temperatures (Figures S17, S18, S21, S22, and S33–S36). For C_2H_2, LIFM-26(Fe[II]/Fe[III]) displays higher isosteric heat (53.8 kJ mol^{-1}) than LIFM-27(Fe[III]) (44.6 kJ mol^{-1}) at near-zero coverage corresponding to the interactions between gas and Fe center, which further confirms the electronic effect of the open Fe[II] centers (Figures S37 and S38). Afterward, the subsequent gradual decrease in isosteric heat for C_2H_2 on both MOFs along with increased C_2H_2 loading amount indicate the adsorption saturation of Fe centers. Notably, the moderate Q_{st} value of C_2H_2 in LIFM-26(Fe[II]/Fe[III]) is lower than some other reported MOFs with OMSs, such as ATC-Cu (79.1 kJ mol^{-1}),[16] Cu@UiO-66(COOH)$_2$ (74.5 kJ mol^{-1}),[43] ZJU-74a (65.0 kJ mol^{-1}),[44] and NKMOF-1-Ni (60.3 kJ mol^{-1}),[45] implying the sufficient adsorption reversibility of the adsorbent owing to the presence of Fe(III) center. For CO_2, both MOFs present comparable isosteric heats, giving values of 37.8 (LIFM-26(Fe[II]/Fe[III])) and 35.8 kJ mol^{-1} (LIFM-27(Fe[III])) at near-zero coverage (Figures S37 and S38). The higher Q_{st} value of C_2H_2 than CO_2 suggests a promising potential of C_2H_2 purification from C_2H_2/CO_2 gas mixture.

Please cite this article in press as: Chen et al., Regulating C_2H_2/CO_2 adsorption selectivity by electronic-state manipulation of iron in metal-organic frameworks, Cell Reports Physical Science (2022), https://doi.org/10.1016/j.xcrp.2022.100977

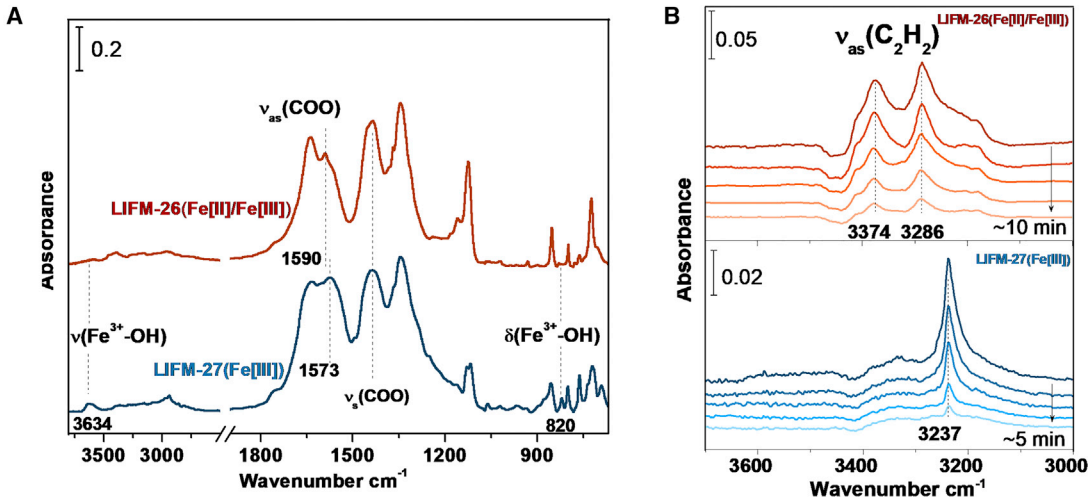

Figure 4. *In situ* IR spectra of LIFM-26(Fe[II]/Fe[III]) and LIFM-27(Fe[III]) before and after C_2H_2 loading

(A) IR spectra of activated LIFM-26(Fe[II]/Fe[III]) (top) and LIFM-27(Fe[III]) (bottom) samples, referenced to pure KBr pellet in vacuum (<20 mTorr base pressure).

(B) Difference spectra showing the asymmetric stretching band vas of adsorbed C_2H_2 in LIFM-26(Fe[II]/Fe[III]) (top) and LIFM-27(Fe[III]) (bottom) samples upon loading at the pressure of ~1 bar (top spectrum in each panel) and subsequent evacuation of gas phase under vacuum for ~10 and ~5 min, respectively. Each is referenced to the spectrum of activated sample.

Adsorption mechanism

To probe the binding interaction of C_2H_2 with the frameworks, *in situ* IR spectroscopy measurements were performed. The samples of LIFM-26(Fe[II]/Fe[III]) and LIFM-27(Fe[III]) were first heated under vacuum to remove trapped solvents and then cooled to room temperature to collect IR spectra of activated samples, as presented in Figure 4A. The spectra of two samples are dominated by the vibrational bands associated with the organic linker (Figure S44), which exhibit general similarities. A noticeable difference is that the LIFM-27(Fe[III]) sample shows extra two bands at ~3,634 and 820 cm^{-1}, which are absent in LIFM-26(Fe[II]/Fe[III]). Based on the well-established studies on Fe-based MOFs containing a hydroxyl group,[46,47] these two bands are attributed to the stretching and deformation modes of OH^-, which terminates one Fe[III] of the trimeric Fe[III]$_3$O cluster for charge balance. In the neutrally charged (Fe[II]/Fe[III])$_3$O cluster of the LIFM-26(Fe[II]/Fe[III]) sample, no extra OH^- is needed. In addition, careful examination of spectra at 1,600–1,500 cm^{-1} reveals that carboxylate asymmetric stretching band ν_{as}(COO) in LIFM-26(Fe[II]/Fe[III]) occurs at a higher frequency (1,590 cm^{-1}) than that in the LIFM-27(Fe[III]) sample, leading to a larger separation $\Delta\nu$ between ν_{as}(COO) and ν_s(COO).[48] This is as expected since the inequivalence of the two C−O bonds connected with Fe[II] and Fe[III], respectively, would further split $\Delta\nu$.[49,50] Gas adsorption measurement was then conducted on these activated samples by loading C_2H_2 at ~1 bar for ~10 min to ensure adsorption saturation, which was followed by subsequent desorption via pumping the samples under vacuum. The adsorbed C_2H_2 is clearly observed in different IR spectra (Figure 4B), which demonstrate the characteristic stretching band $\nu_{as}(C_2H_2)$ of adsorbed C_2H_2 at 3,400–3,200 cm^{-1}. A marked difference is noted for both the position and shape of the $\nu_{as}(C_2H_2)$ band between in LIFM-26(Fe[II]/Fe[III]) and LIFM-27(Fe[III]). LIFM-27(Fe[III]) displays only a single band located at 3,237 cm^{-1}, which corresponds to C_2H_2 adsorbed at the primary exposed Fe[III] sites, as identified by molecular simulations (Figures 5B and S46; vide infra). In comparison, LIFM-26(Fe[II]/Fe[III]) shows two distinct bands appearing at higher frequencies of 3,374 and 3,286 cm^{-1}, pointing to two types of C_2H_2

Please cite this article in press as: Chen et al., Regulating C_2H_2/CO_2 adsorption selectivity by electronic-state manipulation of iron in metal-organic frameworks, Cell Reports Physical Science (2022), https://doi.org/10.1016/j.xcrp.2022.100977

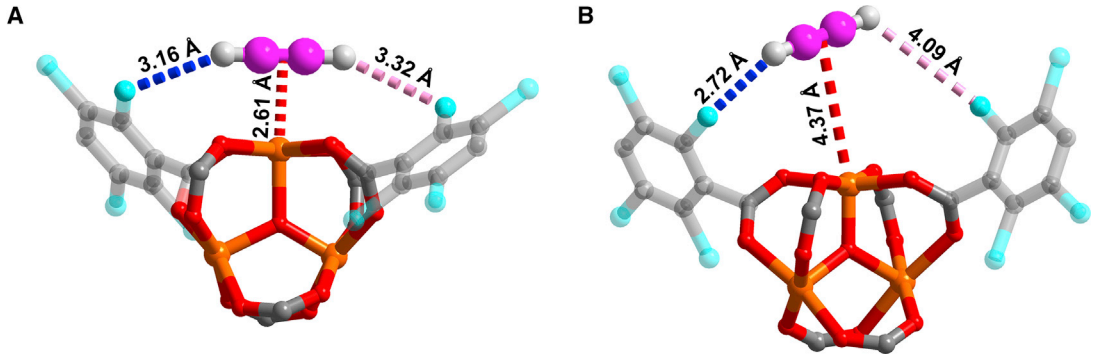

Figure 5. Preferential binding sites
(A and B) The preferential C_2H_2 binding sites in (A) LIFM-26(Fe[II]/Fe[III]) and (B) LIFM-27(Fe[III]).

adsorbed on Fe[II] and Fe[III] sites, respectively. It is noteworthy that the 3,374 cm^{-1} band undergoes an upward shift (blue shift) with respect to the value of the gas phase C_2H_2 (3,287 cm^{-1}).[51] Such a shift to the higher wavenumber strongly suggests that π back donation occurs between Fe[II] cations and C_2H_2 in LIFM-26(Fe[II]/Fe[III]),[52] which weakens the C–C bond but stiffens the C–H bond,[53] thus resulting in a raise of C–H stretching frequency. The broadening and asymmetric line shape of the $\nu_{as}(C_2H_2)$ bands in LIFM-26(Fe[II]/Fe[III]) indicate vibrational dynamic coupling between adsorbed C_2H_2 molecules, which could account for the occurrence of the Fe[III]-bound C_2H_2 band at a higher frequency of 3,286 cm^{-1} in LIFM-26(Fe[II]/Fe[III]) compared with that in LIFM-27(Fe[III]) (3,237 cm^{-1}).[54]

To get further insight into the adsorption mechanism with regard to the mixed-valent Fe[II]/Fe[III] centers, we implemented molecular simulations. For LIFM-26(Fe[II]/Fe[III]), C_2H_2 is mainly located in the channel surrounded by one open Fe[II] center and two chlorine atoms, in which the strong Fe···C≡C (2.61 Å) and weak C-Cl···H interactions (3.16 and 3.22 Å) occur between C_2H_2 and the framework, suggesting strong C_2H_2 binding affinity (Figures 5A and S45), whereas the C_2H_2 binding site in LIFM-27(Fe[III]) is located in the elliptic channel surrounded by one open Fe[III] center and two chlorine atoms with weak Fe··· C≡C (4.37 Å) and C-Cl···H interactions (2.72 and 4.09 Å), indicating weaker C_2H_2 binding affinity compared with LIFM-26(Fe[II]/Fe[III]) (Figures 5B and S46). The calculated C_2H_2 binding energy for LIFM-26(Fe[II]/Fe[III]) is 49.7 kJ mol^{-1}, which is higher than LIFM-27(Fe[III]) (45.6 kJ mol^{-1}) (Table S6), manifesting the stronger interaction between C_2H_2 and LIFM-26(Fe[II]/Fe[III]). In comparison, both LIFM-26(Fe[II]/Fe[III]) and LIFM-27(Fe[III]) present weaker interactions toward CO_2. The observed CO_2 binding site in LIFM-26(Fe[II]/Fe[III]) is mainly the Fe···O-C interaction with a distance of 2.13 Å, which is similar to that of LIFM-27(Fe[III]) (Fe···O-C distance is 2.17 Å) (Figures S47–S49). The CO_2 binding energy for LIFM-26(Fe[II]/Fe[III]) and LIFM-27(Fe[III]) are calculated to be 38.5 and 37.6 kJ mol^{-1}, respectively (Table S6), which are weaker than those of C_2H_2, confirming the feasible C_2H_2/CO_2-separation performance.

IAST adsorption selectivity and dynamic breakthrough

To evaluate the C_2H_2/CO_2-separation ability, the IAST[55] calculation was conducted on the basis of the composition of a 50:50 C_2H_2/CO_2 mixture (Figures S39–S42). As shown in Figures 6A and S43, LIFM-26(Fe[II]/Fe[III]) gives much higher C_2H_2/CO_2 selectivity (56.1 at 0.01 bar) than LIFM-27(Fe[III]) (14.3 at 0.01 bar) under low pressure, which can be attributed to the stronger Fe[II]–C_2H_2 binding affinity as a result

Please cite this article in press as: Chen et al., Regulating C_2H_2/CO_2 adsorption selectivity by electronic-state manipulation of iron in metal-organic frameworks, Cell Reports Physical Science (2022), https://doi.org/10.1016/j.xcrp.2022.100977

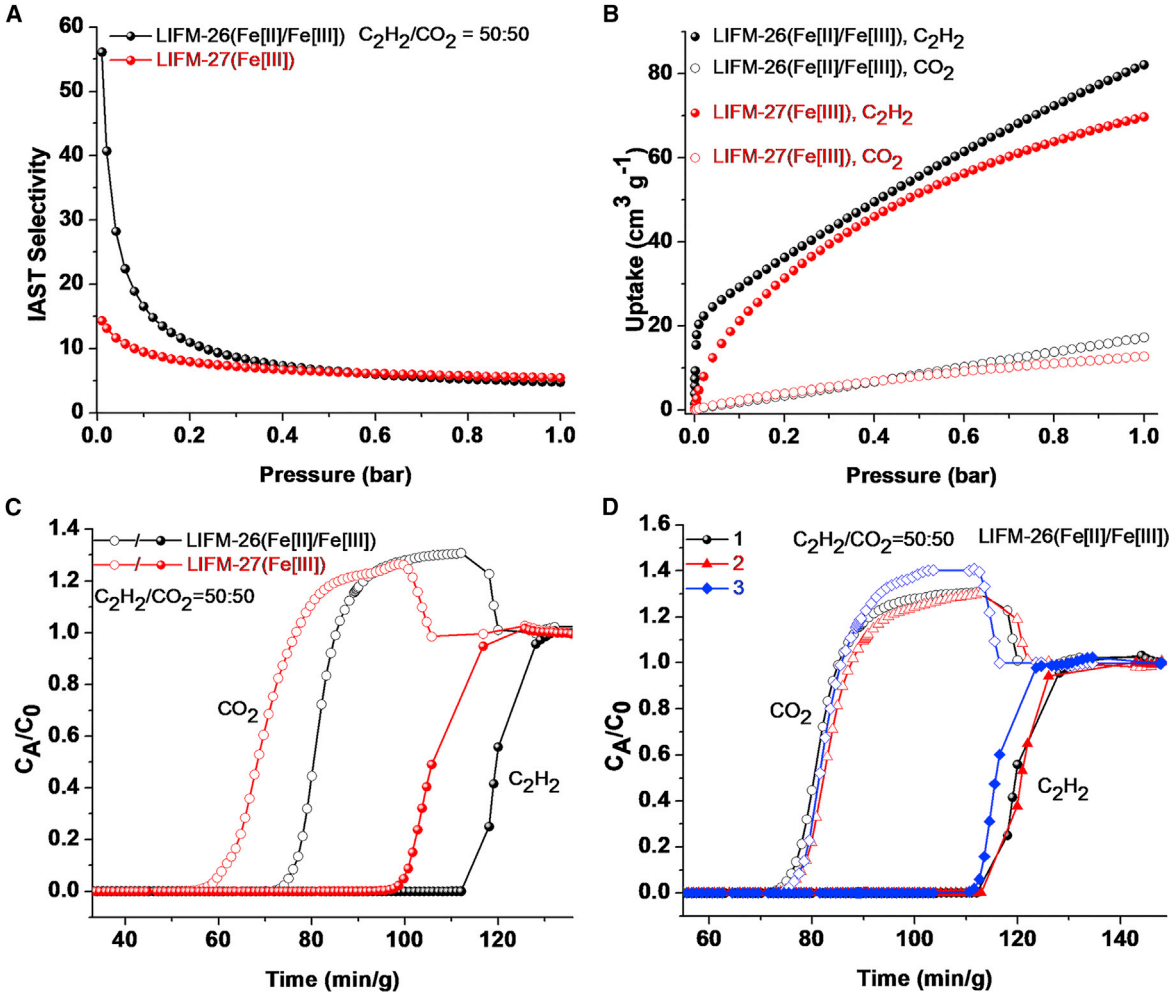

Figure 6. IAST calculated selectivity and dynamic breakthrough

(A) IAST adsorption selectivity of C_2H_2/CO_2 (v/v, 50:50) at 298 K.

(B) IAST calculated C_2H_2 and CO_2 uptake capacity for equimolar C_2H_2/CO_2 mixtures.

(C) The experimental dynamic breakthrough measurements of LIFM-26(Fe[II]/Fe[III]) and LIFM-27(Fe[III]) for C_2H_2/CO_2 mixture at 298 K and 1 bar.

(D) The cycling dynamic breakthrough measurements of LIFM-26(Fe[II]/Fe[III]) for C_2H_2/CO_2 mixture at 298 K and 1 bar.

of the increased electron density at the Fe[II] center. Subsequently, the C_2H_2/CO_2 selectivity for both MOFs gradually decreases as a function of the increased pressure due to the adsorption saturation of the Fe centers. The final C_2H_2/CO_2 selectivities for LIFM-26(Fe[II]/Fe[III]) and LIFM-27(Fe[III]) are 4.8 and 5.5 at 298 K and 1 bar, respectively, which are comparable with many reported MOFs, such as SIFSIX-Cu-TPA (5.3),[41] SNNU-45 (4.5),[56] TIFSIX-2-Cu-i (6.5),[28] FJU-90 (4.3),[42] UTSA-222 (4.0),[57] JNU-1 (3.6),[18] and Zn-MOF-74 (2.8).[31] Additionally, the C_2H_2 uptake capacity was calculated based on the IAST method. Compared with LIFM-27(Fe[III]) (4.7 $cm^3\ g^{-1}$ at 0.01 bar), LIFM-26(Fe[II]/Fe[III]) exhibits enhanced C_2H_2-capture performance, especially at low pressure (20.4 $cm^3\ g^{-1}$ at 0.01 bar) (Figure 6B). More importantly, the C_2H_2 uptake capacity for both MOFs is remarkably higher than their CO_2 adsorption, implying potential C_2H_2-separation ability from C_2H_2/CO_2 mixture (Figure 6B).

Prompted by the outstanding C_2H_2 uptake capacity and C_2H_2/CO_2 adsorption selectivity, the simulated transient breakthrough experiments were carried out

according to the documented methodology.[58] For both LIFM-26(Fe[II]/Fe[III]) and LIFM-27(Fe[III]), CO_2 elutes first, and then C_2H_2 breaks through after some time, demonstrating the adequate capacity for the demanding C_2H_2/CO_2 separation (Figures S52 and S53). The C_2H_2 capture productivity calculated on the basis of the simulated breakthrough curves gives rise to the values of 88.9 (LIFM-26(Fe[II]/Fe[III])) and 76.6 (LIFM-27(Fe[III])) $cm^3\ g^{-1}$, unveiling the better C_2H_2/CO_2-separation performance of LIFM-26(Fe[II]/Fe[III]). It is noticeable that the C_2H_2 productivity for LIFM-26(Fe[II]/Fe[III]) is slightly lower than FJU-90 (114.2 $cm^3\ g^{-1}$)[42] yet higher than other reported MOFs including FJU-22a (83.1 $cm^3\ g^{-1}$),[59] ZUL-60a (80.6 $cm^3\ g^{-1}$),[60] UTSA-74a (79.7 $cm^3\ g^{-1}$),[33] Zn-MOF-74 (76.6 $cm^3\ g^{-1}$),[31] and PCP-33 (75.7 $cm^3\ g^{-1}$).[39]

To further assess the practical C_2H_2/CO_2-separation performance by both LIFM-26(Fe[II]/Fe[III]) and LIFM-27(Fe[III]), dynamic fixed-bed breakthrough experiments were conducted through a stainless-steel column under ambient condition, in which the equimolar C_2H_2/CO_2 mixture flowed over the packed column with a flow rate of 1.0 mL min^{-1}. As depicted in Figure 6C, both Fe-MOFs present excellent C_2H_2-separation performance from C_2H_2/CO_2 mixture. For LIFM-26(Fe[II]/Fe[III]), CO_2 undoubtedly elutes first and then quickly reaches a pure grade without detectable C_2H_2, while C_2H_2 remains in the packed column for a remarkable time until it is saturated in LIFM-26(Fe[II]/Fe[III]). As expected, LIFM-27(Fe[III]) exhibits similar C_2H_2/CO_2 dynamic breakthrough behavior but with a shorter C_2H_2 breakthrough time. Based on the experimental breakthrough curves, LIFM-26(Fe[II]/Fe[III]) and LIFM-27(Fe[III]) present comparable C_2H_2/CO_2 selectivity with values of 1.6 and 1.7, respectively. The calculated C_2H_2-capture productivity for LIFM-26(Fe[II]/Fe[III]) based on the experimental breakthrough curve is estimated to be 60.0 $cm^3\ g^{-1}$, whereas the value for LIFM-27(Fe[III]) is 53.7 $cm^3\ g^{-1}$. In principle, ideal adsorbents should present good recyclability in practical industrial applications. Therefore, the continuous dynamic breakthrough experiments were performed under the above conditions. The results indicate that both Fe-MOFs maintain almost the same retaining time and capture productivity in three continuous C_2H_2/CO_2 dynamic breakthrough experiments (Figures 6D, S50, and S51), demonstrating their good reusability. The PXRD patterns after the repetitive experiments also confirm the crystallinity is retained well (Figures S54 and S55). Taken together, these results clearly demonstrate that the Fe-MOFs have successfully achieved a combination of high C_2H_2 uptake capacity, moderate-high C_2H_2/CO_2 selectivity, and sufficient reversibility by rationally regulating the electronic state of the open-metal centers.

In summary, a metal electronic-state manipulation strategy has been successfully applied to constructing a pair of microporous isostructural Fe-MOFs featuring open Fe centers with different electron densities for efficient C_2H_2/CO_2 separation. Notably, the isostructural LIFM-26(Fe[II]/Fe[III]) and LIFM-27(Fe[III]) can be interconverted, and the electronic state of Fe centers can be finely tuned by simply changing the oxidation conditions depending on the solvents and reaction time, thus facilitating understanding of the inherent relationship between the metal electronic state and C_2H_2 selective adsorption. Compared with LIFM-27(Fe[III]), LIFM-26(Fe[II]/Fe[III]) presents remarkably higher C_2H_2 uptake capacity while retaining moderate-high C_2H_2/CO_2 selectivity, which is well supported by the simulated and experimental dynamic breakthrough experiments. *In situ* IR and molecular calculations manifest that LIFM-26(Fe[II]/Fe[III]) exhibits enhanced binding affinity toward C_2H_2 than LIFM-27(Fe[III]) due to the increased electron density at the metal site, resulting in a stronger π back donation. Significantly, this work provides an effective guideline to realize the challenging C_2H_2/CO_2 separation by rationally manipulating the electronic state of OMSs in MOF pore spaces.

Please cite this article in press as: Chen et al., Regulating C_2H_2/CO_2 adsorption selectivity by electronic-state manipulation of iron in metal-organic frameworks, Cell Reports Physical Science (2022), https://doi.org/10.1016/j.xcrp.2022.100977

MATERIALS AND METHODS

See the supplemental experimental procedures for full details of synthesis, characterization, modeling and analysis, and adsorption and breakthrough measurements.

EXPERIMENTAL PROCEDURES

Resource availability

Lead contact

Further information and requests for resources should be directed to and will be fulfilled by the lead contact, Cheng-Yong Su (cesscy@mail.sysu.edu.cn), and Shengqian Ma (shengqian.ma@unt.edu).

Materials availability

All materials generated in this study are available from the lead contact without restriction.

Data and code availability

The X-ray crystallographic coordinates for LIFM-27(Fe[III]) have been deposited at the Cambridge Crystallographic Data Centre (CCDC) under CCDC: 2114493. These data can be obtained free of charge from the CCDC via http://www.ccdc.cam.ac.uk/data_request/cif. All other data are available from the lead contact upon request.

SUPPLEMENTAL INFORMATION

Supplemental information can be found online at https://doi.org/10.1016/j.xcrp.2022.100977.

ACKNOWLEDGMENTS

This work was supported by NSFC (21821003, 21890380, and 22001271), the Chinese Postdoctoral Science Foundation (2017M622866), the International Postdoctoral Exchange Fellowship Program (20180055), and FRF for the Central Universities (20lgpy79). The authors also extend their appreciation to the Robert A. Welch Foundation (B-0027) and Researchers Supporting Program (RSP-2022/55) at King Saud University, Riyadh, Saudi Arabia, for partial support of this work. T.P. and K.A.F. acknowledge the use of services provided by Research Computing at the University of South Florida. The IR spectroscopic work was supported by the US Department of Energy, Office of Science, Basic Energy Sciences, under award no. DE-SC0019902.

AUTHOR CONTRIBUTIONS

Conceptualization, C.-X.C., C.-Y.S., and S.M.; methodology, C.-X.C.; investigation, C.-X.C.; theoretical calculation, T.P. and K.A.F.; *in situ* IR measurements, K.T.; simulated transient breakthrough, R.K.; Mössbauer spectra, S.C. and L.W.; writing – original draft, C.-X.C.; writing – review & editing, C.-X.C., H.W., S.M., and C.-Y.S.; funding acquisition, C.-X.C., C.-Y.S., and S.M.; all authors analyzed and discussed the data and contributed to writing the paper.

DECLARATION OF INTERESTS

The authors declare no competing interests.

Received: April 14, 2022
Revised: June 3, 2022
Accepted: June 17, 2022
Published: July 20, 2022

REFERENCES

1. Sholl, D.S., and Lively, R.P. (2016). Seven chemical separations to change the world. Nature *532*, 435–437. https://doi.org/10.1038/532435a.

2. Guo, C.J., Shen, D., and Bülow, M. (2001). 18-O-03-Kinetic separation of binary mixtures of carbon dioxide and C_2 hydrocarbons on modified LTA-type zeolites. In Studies in Surface Science and Catalysis, A. Galarneau, F. Fajula, F. Di Renzo, and J. Vedrine, eds. (Elsevier), p. 144.

3. Pässler, P., Hefner, W., Buckl, K., Meinass, H., Meiswinkel, A., Wernicke, H.-J., Ebersberg, G., Müller, R., Bässler, J., Behringer, H., and Mayer, D. (2011). In Ullmann's Encyclopedia of Industrial Chemistry, B. Elvers, ed. (Wiley-VCH).

4. Duan, X., Cai, J., Yu, J., Wu, C., Cui, Y., Yang, Y., and Qian, G. (2013). Three-dimensional copper (II) metal–organic framework with open metal sites and anthracene nucleus for highly selective C_2H_2/CH_4 and C_2H_2/CO_2 gas separation at room temperature. Microporous Mesoporous Mater. *181*, 99–104. https://doi.org/10.1016/j.micromeso.2013.07.019.

5. Reid, C.R., and Thomas, K.M. (2001). Adsorption kinetics and size exclusion properties of probe molecules for the selective porosity in a carbon molecular sieve used for air separation. J. Phys. Chem. B *105*, 10619–10629. https://doi.org/10.1021/jp0108263.

6. Adil, K., Belmabkhout, Y., Pillai, R.S., Cadiau, A., Bhatt, P.M., Assen, A.H., Maurin, G., and Eddaoudi, M. (2017). Gas/vapour separation using ultra-microporous metal-organic frameworks: insights into the structure/separation relationship. Chem. Soc. Rev. *46*, 3402–3430. https://doi.org/10.1039/c7cs00153c.

7. Shekhah, O., Chernikova, V., Belmabkhout, Y., and Eddaoudi, M. (2018). Metal–organic framework membranes: from fabrication to gas separation. Crystals *8*, 412. https://doi.org/10.3390/cryst8110412.

8. Yang, L., Qian, S., Wang, X., Cui, X., Chen, B., and Xing, H. (2020). Energy-efficient separation alternatives: metal-organic frameworks and membranes for hydrocarbon separation. Chem. Soc. Rev. *49*, 5359–5406. https://doi.org/10.1039/c9cs00756c.

9. Li, J., Bhatt, P.M., Li, J., Eddaoudi, M., and Liu, Y. (2020). Recent progress on microfine design of metal-organic frameworks: structure regulation and gas sorption and separation. Adv. Mater. *32*, 2002563. https://doi.org/10.1002/adma.202002563.

10. Wang, H., Liu, Y., and Li, J. (2020). Designer metal-organic frameworks for size-exclusion-based hydrocarbon separations: progress and challenges. Adv. Mater. *32*, 2002603. https://doi.org/10.1002/adma.202002603.

11. Lin, R.-B., Xiang, S., Zhou, W., and Chen, B. (2020). Microporous metal-organic framework materials for gas separation. Chem *6*, 337–363. https://doi.org/10.1016/j.chempr.2019.10.012.

12. Hua, G.F., Xie, X.J., Lu, W., and Li, D. (2020). Optimizing supramolecular interactions in metal-organic frameworks for C_2 separation. Dalton Trans. *49*, 15548–15559. https://doi.org/10.1039/d0dt03013a.

13. Cui, W.G., Hu, T.L., and Bu, X.H. (2020). Metal-organic framework materials for the separation and purification of light hydrocarbons. Adv. Mater. *32*, 1806445. https://doi.org/10.1002/adma.201806445.

14. Oktawiec, J., Jiang, H.Z.H., Vitillo, J.G., Reed, D.A., Darago, L.E., Trump, B.A., Bernales, V., Li, H., Colwell, K.A., Furukawa, H., et al. (2020). Negative cooperativity upon hydrogen bond-stabilized O2 adsorption in a redox-active metal-organic framework. Nat. Commun. *11*, 3087. https://doi.org/10.1038/s41467-020-16897-z.

15. Reed, D.A., Xiao, D.J., Gonzalez, M.I., Darago, L.E., Herm, Z.R., Grandjean, F., and Long, J.R. (2016). Reversible CO scavenging via adsorbate-dependent spin state transitions in an iron(II)-Triazolate metal-organic framework. J. Am. Chem. Soc. *138*, 5594–5602. https://doi.org/10.1021/jacs.6b00248.

16. Niu, Z., Cui, X., Pham, T., Verma, G., Lan, P.C., Shan, C., Xing, H., Forrest, K.A., Suepaul, S., Space, B., et al. (2021). A MOF-based ultra-strong acetylene nano-trap for highly efficient C_2H_2/CO_2 separation. Angew. Chem. Int. Ed. *60*, 5283–5288. https://doi.org/10.1002/anie.202016225.

17. Di, Z., Liu, C., Pang, J., Chen, C., Hu, F., Yuan, D., Wu, M., and Hong, M. (2021). Cage-like porous materials with simultaneous high C_2H_2 storage and excellent C_2H_2/CO_2 separation performance. Angew. Chem. Int. Ed. *60*, 10828–10832. https://doi.org/10.1002/anie.202101907.

18. Zeng, H., Xie, M., Huang, Y.L., Zhao, Y., Xie, X.J., Bai, J.P., Wan, M.Y., Krishna, R., Lu, W., and Li, D. (2019). Induced fit of C_2H_2 in a flexible MOF through cooperative action of open metal sites. Angew. Chem. Int. Ed. *58*, 8515–8519. https://doi.org/10.1002/anie.201904160.

19. Fischer, M., Hoffmann, F., and Fröba, M. (2010). New microporous materials for acetylene storage and C_2H_2/CO_2 separation: insights from molecular simulations. ChemPhysChem *11*, 2220–2229. https://doi.org/10.1002/cphc.201000126.

20. Xu, H., He, Y., Zhang, Z., Xiang, S., Cai, J., Cui, Y., Yang, Y., Qian, G., and Chen, B. (2013). A microporous metal–organic framework with both open metal and Lewis basic pyridyl sites for highly selective C2H2/CH4and C_2H_2/CO_2 gas separation at room temperature. J. Mater. Chem. *1*, 77–81. https://doi.org/10.1039/c2ta00155a.

21. Ji, Y., Ding, L., Cheng, Y., Zhou, H., Yang, S., Li, F., and Li, Y. (2017). Understanding the effect of ligands on C2H2 storage and C_2H_2/CH_4, C_2H_2/CO_2 separation in metal–organic frameworks with open Cu(II) sites. J. Phys. Chem. C *121*, 24104–24113.

22. Moreau, F., da Silva, I., Al Smail, N.H., Easun, T.L., Savage, M., Godfrey, H.G.W., Parker, S.F., Manuel, P., Yang, S., and Schröder, M. (2017). Unravelling exceptional acetylene and carbon dioxide adsorption within a tetra-amide functionalized metal-organic framework. Nat. Commun. *8*, 14085. https://doi.org/10.1038/ncomms14085.

23. Chen, S., Behera, N., Yang, C., Dong, Q., Zheng, B., Li, Y., Tang, Q., Wang, Z., Wang, Y., and Duan, J. (2020). A chemically stable nanoporous coordination polymer with fixed and free Cu^{2+} ions for boosted C_2H_2/CO_2 separation. Nano Res. *14*, 546–553. https://doi.org/10.1007/s12274-020-2935-1.

24. Pang, J., Jiang, F., Wu, M., Liu, C., Su, K., Lu, W., Yuan, D., and Hong, M. (2015). A porous metal-organic framework with ultrahigh acetylene uptake capacity under ambient conditions. Nat. Commun. *6*, 7575. https://doi.org/10.1038/ncomms8575.

25. Lin, R.-B., Li, L., Wu, H., Arman, H., Li, B., Lin, R.-G., Zhou, W., and Chen, B. (2017). Optimized separation of acetylene from carbon dioxide and ethylene in a microporous material. Material. J. Am. Chem. Soc. *139*, 8022–8028. https://doi.org/10.1021/jacs.7b03850.

26. Bloch, E.D., Queen, W.L., Krishna, R., Zadrozny, J.M., Brown, C.M., and Long, J.R. (2012). Hydrocarbon separations in a metal-organic framework with open iron(II) coordination sites. Science *335*, 1606–1610. https://doi.org/10.1126/science.1217544.

27. Zhang, J.-P., and Chen, X.-M. (2009). Optimized acetylene/carbon dioxide sorption in a dynamic porous crystal. J. Am. Chem. Soc. *131*, 5516–5521. https://doi.org/10.1021/ja8089872.

28. Chen, K.-J., Scott, H.S., Madden, D.G., Pham, T., Kumar, A., Bajpai, A., Lusi, M., Forrest, K.A., Space, B., Perry, J.J., and Zaworotko, M.J. (2016). Benchmark C_2H_2/CO_2 and CO_2/C_2H_2 separation by two closely related hybrid ultra-microporous materials. Chem *1*, 753–765. https://doi.org/10.1016/j.chempr.2016.10.009.

29. Cui, X., Chen, K., Xing, H., Yang, Q., Krishna, R., Bao, Z., Wu, H., Zhou, W., Dong, X., Han, Y., et al. (2016). Pore chemistry and size control in hybrid porous materials for acetylene capture from ethylene. Science *353*, 141–144. https://doi.org/10.1126/science.aaf2458.

30. Fan, W., Yuan, S., Wang, W., Feng, L., Liu, X., Zhang, X., Wang, X., Kang, Z., Dai, F., Yuan, D., et al. (2020). Optimizing multivariate metal-organic frameworks for efficient C_2H_2/CO_2 separation. J. Am. Chem. Soc. *142*, 8728–8737. https://doi.org/10.1021/jacs.0c00805.

31. Xiang, S., Zhou, W., Zhang, Z., Green, M.A., Liu, Y., and Chen, B. (2010). Open metal sites within isostructural metal-organic frameworks for differential recognition of acetylene and extraordinarily high acetylene storage capacity at room temperature. Angew. Chem. Int. Ed. *49*, 4615–4618. https://doi.org/10.1002/anie.201000094.

32. Yoon, J.W., Lee, J.S., Lee, S., Cho, K.H., Hwang, Y.K., Daturi, M., Jun, C.H., Krishna, R., and Chang, J.S. (2015). Adsorptive separation of acetylene from light hydrocarbons by mesoporous iron trimesate MIL-100(Fe). Chem. Eur J. *21*, 18431–18438. https://doi.org/10.1002/chem.201502893.

33. Luo, F., Yan, C., Dang, L., Krishna, R., Zhou, W., Wu, H., Dong, X., Han, Y., Hu, T.L., O'Keeffe,

M., et al. (2016). UTSA-74: a MOF-74 isomer with two accessible binding sites per metal center for highly selective gas separation. J. Am. Chem. Soc. *138*, 5678–5684. https://doi.org/10.1021/jacs.6b02030.

34. Yoon, J.W., Seo, Y.K., Hwang, Y.K., Chang, J.S., Leclerc, H., Wuttke, S., Bazin, P., Vimont, A., Daturi, M., Bloch, E., et al. (2010). Controlled reducibility of a metal-organic framework with coordinatively unsaturated sites for preferential gas sorption. Angew. Chem. Int. Ed. *49*, 5949–5952. https://doi.org/10.1002/anie.201001230.

35. Bachman, J.E., Kapelewski, M.T., Reed, D.A., Gonzalez, M.I., and Long, J.R. (2017). M_2(m-dobdc) (M = Mn, Fe, Co, Ni) metal-organic frameworks as highly selective, high-capacity adsorbents for olefin/paraffin separations. J. Am. Chem. Soc. *139*, 15363–15370. https://doi.org/10.1021/jacs.7b06397.

36. Luna-Triguero, A., Vicent-Luna, J.M., Madero-Castro, R.M., Gómez-Álvarez, P., and Calero, S. (2019). Acetylene storage and separation using metal-organic frameworks with open metal sites. ACS Appl. Mater. Interfaces *11*, 31499–31507. https://doi.org/10.1021/acsami.9b09010.

37. Chen, C.X., Zheng, S.P., Wei, Z.W., Cao, C.C., Wang, H.P., Wang, D.W., Jiang, J.J., Fenske, D.T., and Su, C.Y. (2017). A robust metal-organic framework combining open metal sites and polar groups for methane purification and CO_2/fluorocarbon capture. Chem. Eur J. *23*, 4060–4064. https://doi.org/10.1002/chem.201606038.

38. Yoon, J.H., Choi, S.B., Oh, Y.J., Seo, M.J., Jhon, Y.H., Lee, T.-B., Kim, D., Choi, S.H., and Kim, J. (2007). A porous mixed-valent iron MOF exhibiting the acs net: synthesis, characterization and sorption behavior of $Fe_3O(F_4BDC)_3(H_2O)_3\cdot(DMF)_{3.5}$. Catal. Today *120*, 324–329. https://doi.org/10.1016/j.cattod.2006.09.003.

39. Duan, J., Jin, W., and Krishna, R. (2015). Natural gas purification using a porous coordination polymer with water and chemical stability. Inorg. Chem. *54*, 4279–4284. https://doi.org/10.1021/ic5030058.

40. Ye, Y., Xian, S., Cui, H., Tan, K., Gong, L., Liang, B., Pham, T., Pandey, H., Krishna, R., Lan, P.C., et al. (2022). Metal–organic framework based hydrogen-bonding nanotrap for efficient acetylene storage and separation. J. Am. Chem. Soc. *144*, 1681–1689. https://doi.org/10.1021/jacs.1c10620.

41. Li, H., Liu, C., Chen, C., Di, Z., Yuan, D., Pang, J., Wei, W., Wu, M., and Hong, M. (2021). An unprecedented pillar-cage fluorinated hybrid porous framework with highly efficient acetylene storage and separation. Angew. Chem. Int. Ed. *60*, 7547–7552. https://doi.org/10.1002/anie.202013988.

42. Ye, Y., Ma, Z., Lin, R.B., Krishna, R., Zhou, W., Lin, Q., Zhang, Z., Xiang, S., and Chen, B. (2019). Pore space partition within a metal-organic framework for highly efficient C_2H_2/CO_2 separation. J. Am. Chem. Soc. *141*, 4130–4136. https://doi.org/10.1021/jacs.9b00232.

43. Zhang, L., Jiang, K., Yang, L., Li, L., Hu, E., Yang, L., Shao, K., Xing, H., Yang, Y., Cui, Y., et al. (2021). Benchmark C_2H_2/CO_2 separation in an ultramicroporous metal–organic framework via copper(I)-Alkynyl chemistry. Angew. Chem. Int. Ed. *60*, 15995–16002. https://doi.org/10.1002/anie.202102810.

44. Pei, J., Shao, K., Wang, J.X., Wen, H.M., Yang, Y., Cui, Y., Krishna, R., Li, B., and Qian, G. (2020). A chemically stable hofmann-type metal-organic framework with sandwich-like binding sites for benchmark acetylene capture. Adv. Mater. *32*, 1908275. https://doi.org/10.1002/adma.201908275.

45. Peng, Y.-L., Pham, T., Li, P., Wang, T., Chen, Y., Chen, K.-J., Forrest, K.A., Space, B., Cheng, P., Zaworotko, M.J., and Zhang, Z. (2018). Robust ultramicroporous metal–organic frameworks with BenchmarkAffinity forAcetylene. Angew. Chem. Int. Ed. *57*, 10971–10975. https://doi.org/10.1002/anie.201806732.

46. Xiao, D.J., Bloch, E.D., Mason, J.A., Queen, W.L., Hudson, M.R., Planas, N., Borycz, J., Dzubak, A.L., Verma, P., Lee, K., et al. (2014). Oxidation of ethane to ethanol by N2O in a metal–organic framework with coordinatively unsaturated iron(II) sites. Nat. Chem. *6*, 590–595. https://doi.org/10.1038/nchem.1956.

47. Devic, T., Horcajada, P., Serre, C., Salles, F., Maurin, G., Moulin, B., Heurtaux, D., Clet, G., Vimont, A., Grenèche, J.M., et al. (2010). Functionalization in flexible porous solids: effects on the pore opening and the Host−Guest interactions. J. Am. Chem. Soc. *132*, 1127–1136. https://doi.org/10.1021/ja9092715.

48. Deacon, G.B., and Phillips, R.J. (1980). Relationships between the carbon-oxygen stretching frequencies of carboxylato complexes and the type of carboxylate coordination. Coord. Chem. Rev. *33*, 227–250. https://doi.org/10.1016/s0010-8545(00)80455-5.

49. Nakamoto, K. (2009). Infrared and Raman Spectra of Inorganic and Coordination Compounds, Sixth edition (Wiley & Sons, Inc.).

50. Colthup, N.B., Daly, L.H., and Wiberley, S.E. (1990). Introduction to Infrared and Raman Spectroscopy, Third edition (Academic Press).

51. Kumar, N., Mukherjee, S., Harvey-Reid, N.C., Bezrukov, A.A., Tan, K., Martins, V., Vandichel, M., Pham, T., van Wyk, L.M., Oyekan, K., et al. (2021). Breaking the trade-off between selectivity and adsorption capacity for gas separation. Chem *7*, 3085–3098. https://doi.org/10.1016/j.chempr.2021.07.007.

52. Citek, C., Oyala, P.H., and Peters, J.C. (2019). Mononuclear Fe(I) and Fe(II) acetylene adducts and their reductive protonation to terminal Fe(IV) and Fe(V) carbynes. J. Am. Chem. Soc. *141*, 15211–15221. https://doi.org/10.1021/jacs.9b06987.

53. Lamberti, C., Zecchina, A., Groppo, E., and Bordiga, S. (2010). Probing the surfaces of heterogeneous catalysts by in situ IR spectroscopy. Chem. Soc. Rev. *39*, 4951. https://doi.org/10.1039/c0cs00117a.

54. Tobin, R.G. (1987). Vibrational linewidths of adsorbed molecules: experimental considerations and results. Surf. Sci. *183*, 226–250. https://doi.org/10.1016/s0039-6028(87)80347-3.

55. Myers, A.L., and Prausnitz, J.M. (1965). Thermodynamics of mixed-gas adsorption. AIChE J. *11*, 121–127. https://doi.org/10.1002/aic.690110125.

56. Li, Y.P., Wang, Y., Xue, Y.Y., Li, H.P., Zhai, Q.G., Li, S.N., Jiang, Y.C., Hu, M.C., and Bu, X. (2019). Ultramicroporous building units as a path to Bi-microporous metal-organic frameworks with high acetylene storage and separation performance. Angew. Chem. Int. Ed. *58*, 13590–13595. https://doi.org/10.1002/anie.201908378.

57. Ma, J.X., Guo, J., Wang, H., Li, B., Yang, T., and Chen, B. (2017). Microporous lanthanide metal-organic framework constructed from lanthanide metalloligand for selective separation of C2H2/CO2 and C2H2/CH4 at room temperature. Inorg. Chem. *56*, 7145–7150. https://doi.org/10.1021/acs.inorgchem.7b00762.

58. Krishna, R. (2017). Screening metal–organic frameworks for mixture separations in fixed-bed adsorbers using a combined selectivity/capacity metric. RSC Adv. *7*, 35724–35737. https://doi.org/10.1039/c7ra07363a.

59. Yao, Z., Zhang, Z., Liu, L., Li, Z., Zhou, W., Zhao, Y., Han, Y., Chen, B., Krishna, R., and Xiang, S. (2016). Extraordinary separation of acetylene-containing mixtures with microporous metal–organic frameworks with open O donor sites and tunable robustness through control of the helical chain secondary building units. Chem. Eur J. *22*, 5676–5683. https://doi.org/10.1002/chem.201505107.

60. Duan, X., Zhang, Q., Cai, J., Yang, Y., Cui, Y., He, Y., Wu, C., Krishna, R., Chen, B., and Qian, G. (2014). A new metal–organic framework with potential for adsorptive separation of methane from carbon dioxide, acetylene, ethylene, and ethane established by simulated breakthrough experiments. J. Mater. Chem. *2*, 2628. https://doi.org/10.1039/c3ta14454b.

Cell Reports Physical Science, Volume *3*

Supplemental information

Regulating C_2H_2/CO_2 adsorption selectivity by electronic-state manipulation of iron in metal-organic frameworks

Cheng-Xia Chen, Tony Pham, Kui Tan, Rajamani Krishna, Pui Ching Lan, Longfei Wang, Songbo Chen, Abdullah M. Al-Enizi, Ayman Nafady, Katherine A. Forrest, Haiping Wang, Sicheng Wang, Chuan Shan, Lei Zhang, Cheng-Yong Su, and Shengqian Ma

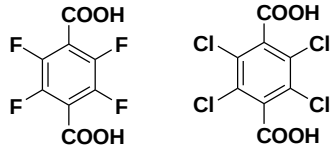

Scheme S1. The structure of ligand.

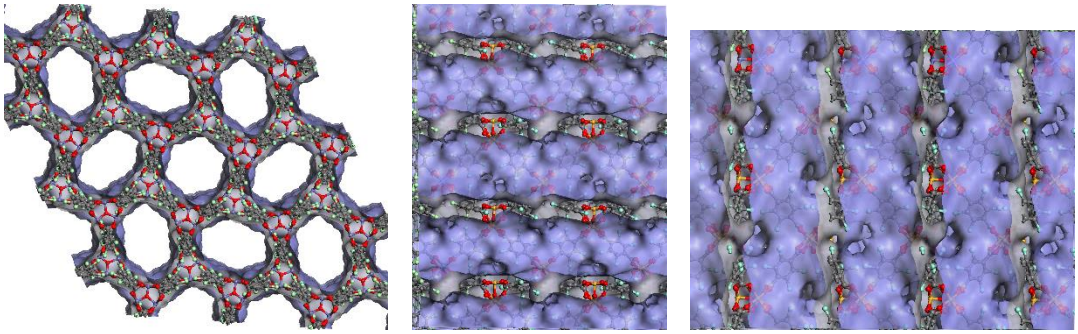

Figure S1. The pore geometry of LIFM-26(Fe[II]/Fe[III]).

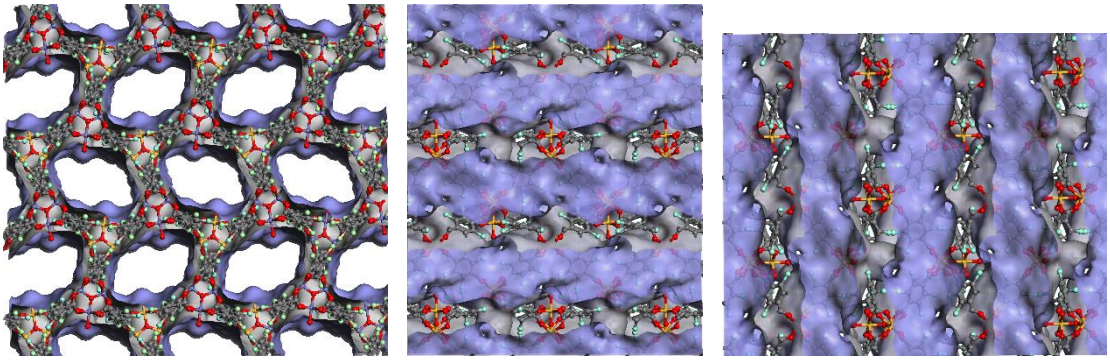

Figure S2. The pore geometry of LIFM-27(Fe[III]).

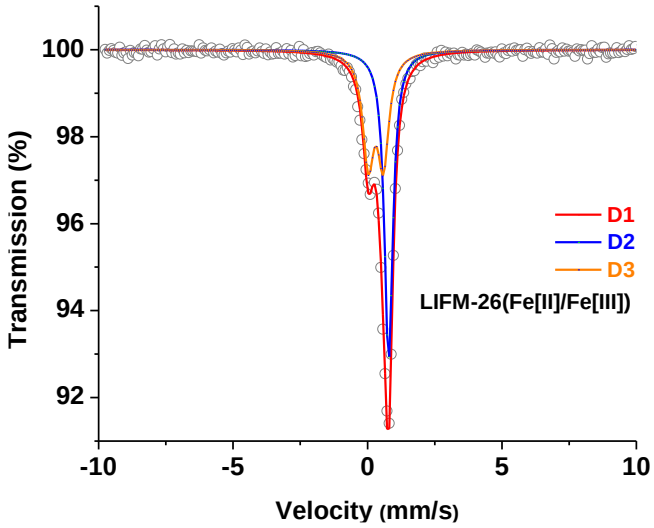

Figure S3. The mösbauer spectrum of LIFM-26(Fe[II]/Fe[III]).

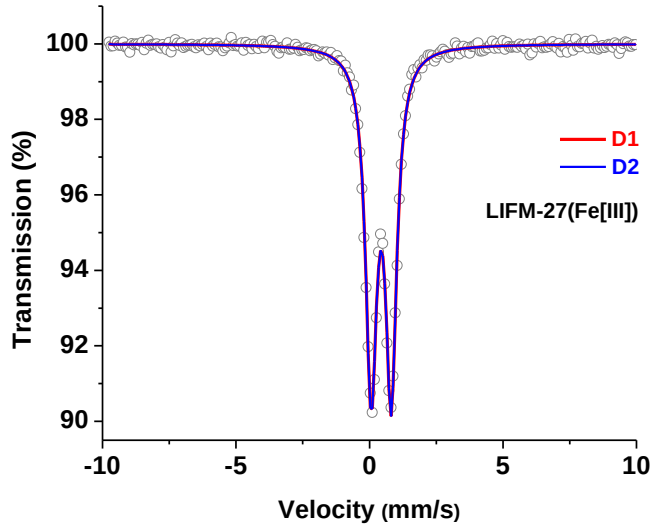

Figure S4. The mösbauer spectrum of LIFM-27(Fe[III]).

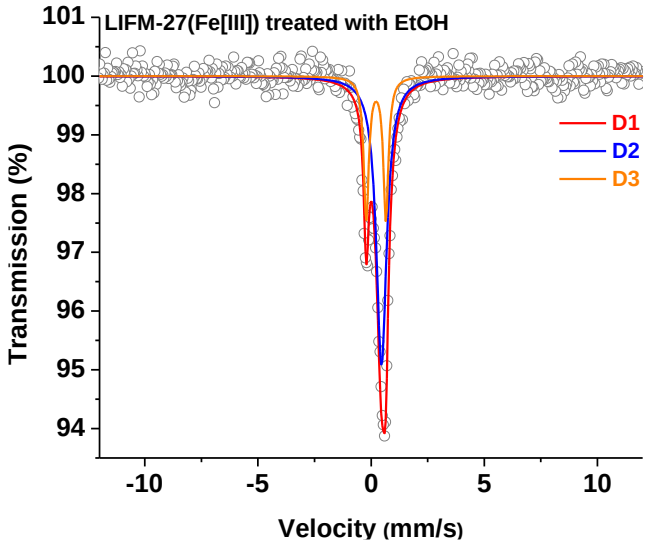

Figure S5. The mösbauer spectrum of LIFM-27(Fe[III])-EtOH.

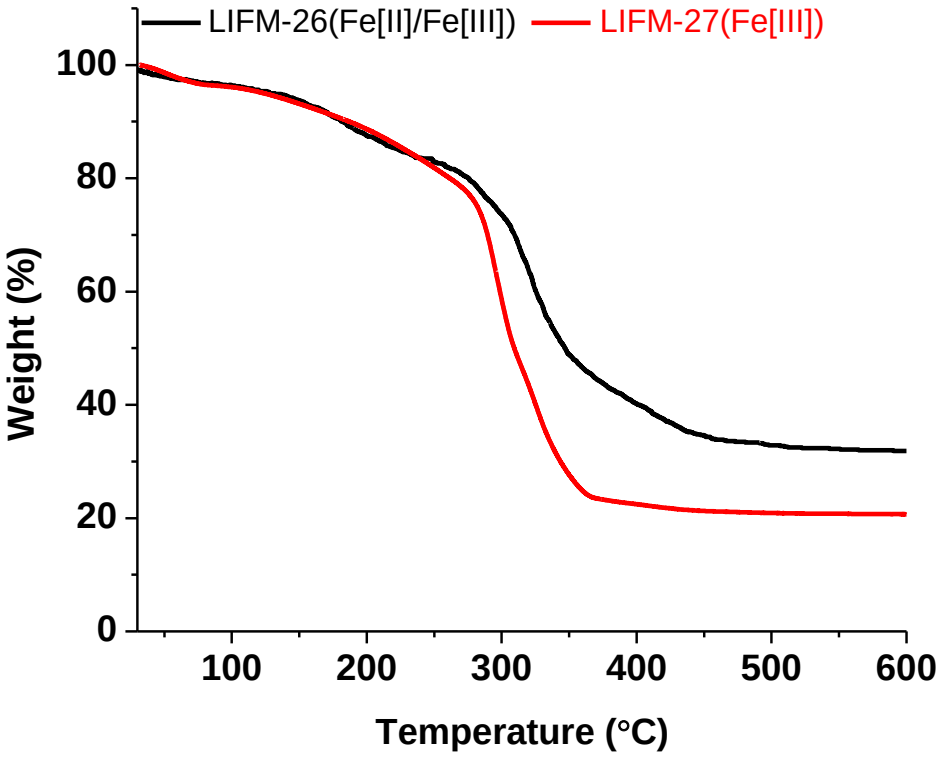

Figure S6. The thermogravimetric analysis of LIFM-26(Fe[II]/Fe[III]) and LIFM-27(Fe[III]).

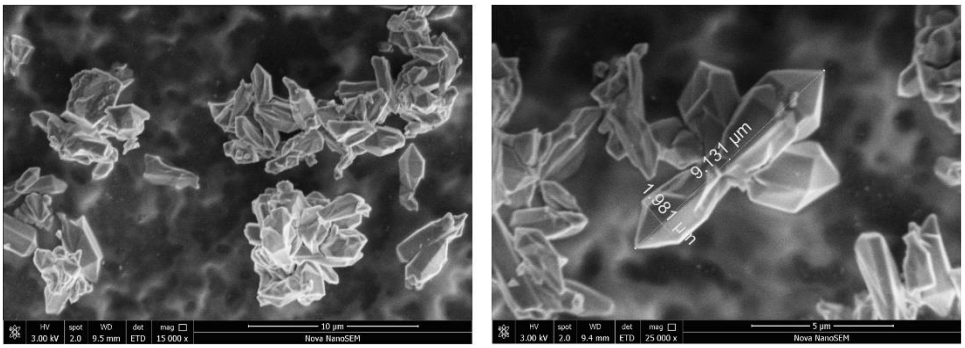

LIFM-26(Fe[II]/Fe[III])

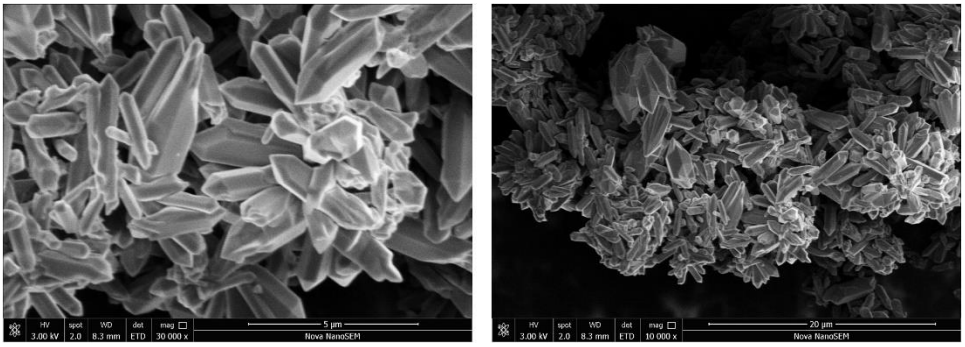

LIFM-27(Fe[III])

Figure S7. The Scanning electron microscopy images of LIFM-26(Fe[II]/Fe[III]) and LIFM-27(Fe[III]).

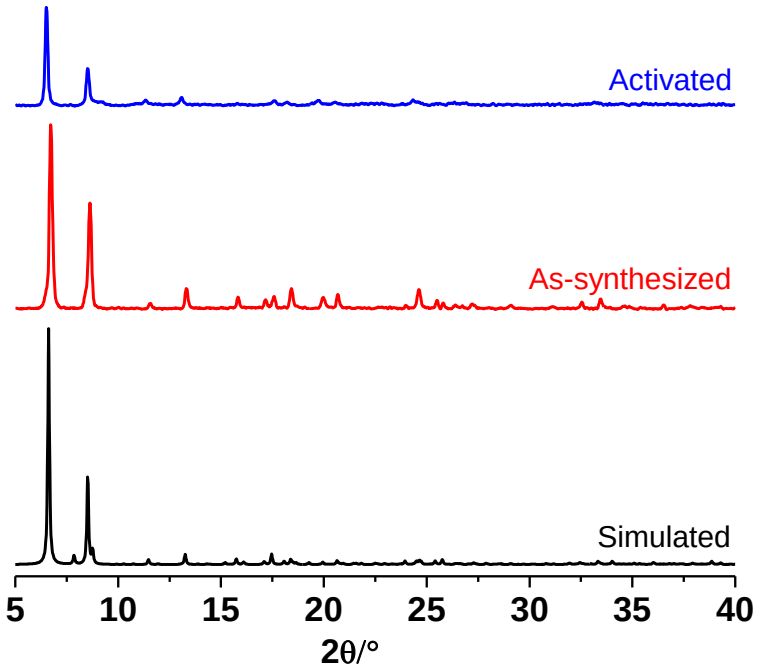

Figure S8. The PXRD pattern of LIFM-26(Fe[II]/Fe[III]).

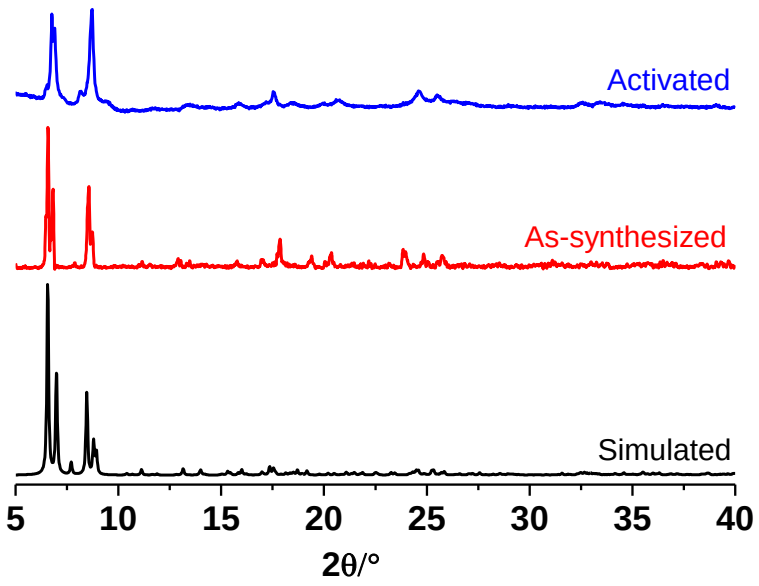

Figure S9. The PXRD pattern of LIFM-27(Fe[III]).

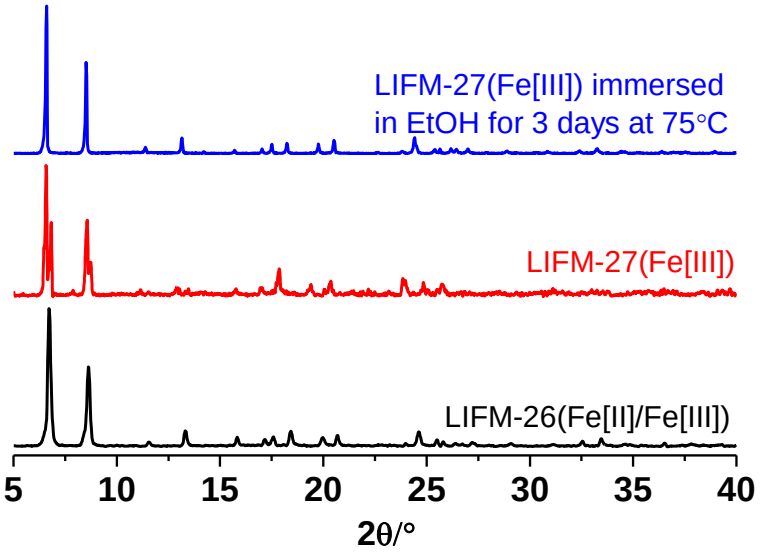

Figure S10. The transformation from LIFM-27(Fe[III]) to LIFM-26(Fe[II]/Fe[III]).

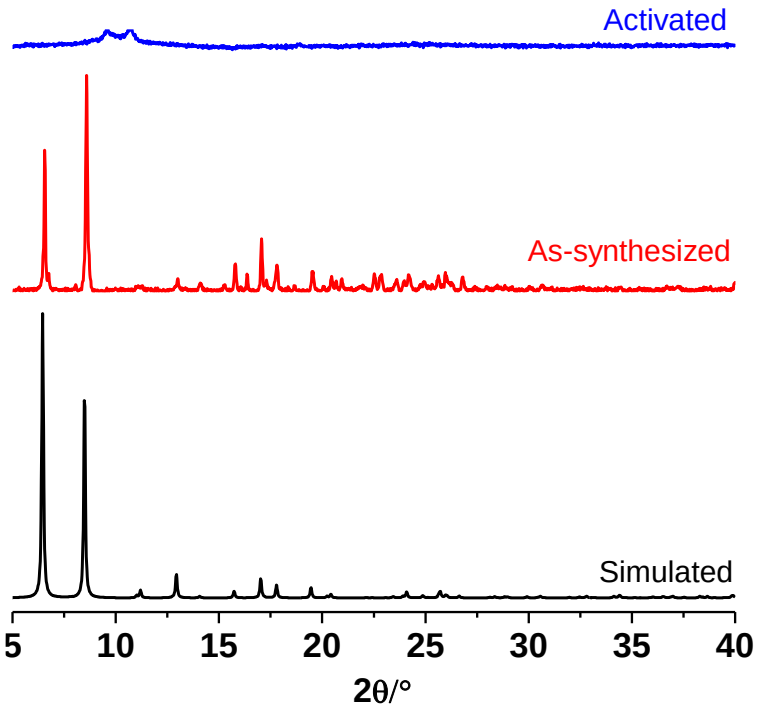

Figure S11. The PXRD patterns of $(Fe[II]/Fe[III])_3O(TFBDC)_3$.

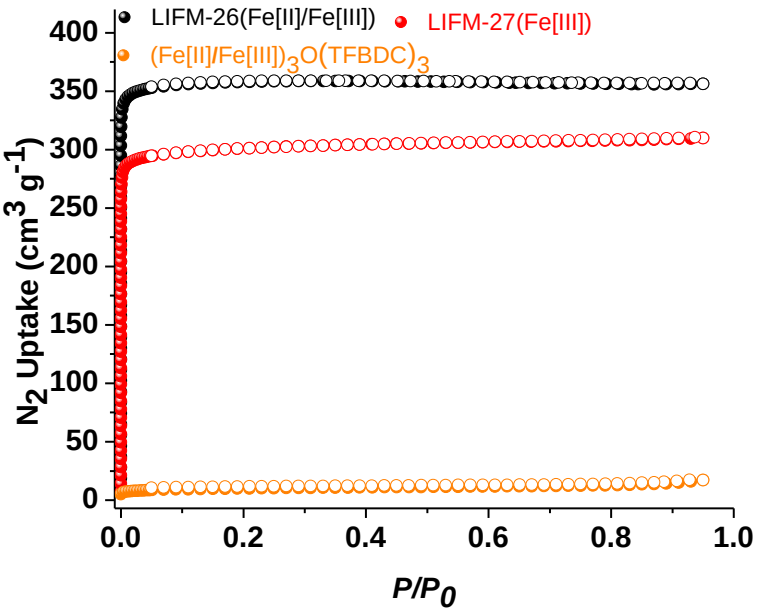

Figure S12. The N_2 (77 K) adsorption isotherms of LIFM-26(Fe[II]/Fe[III]), LIFM-27(Fe[III]), and (Fe[II]/Fe[III])$_3$O(TFBDC)$_3$.

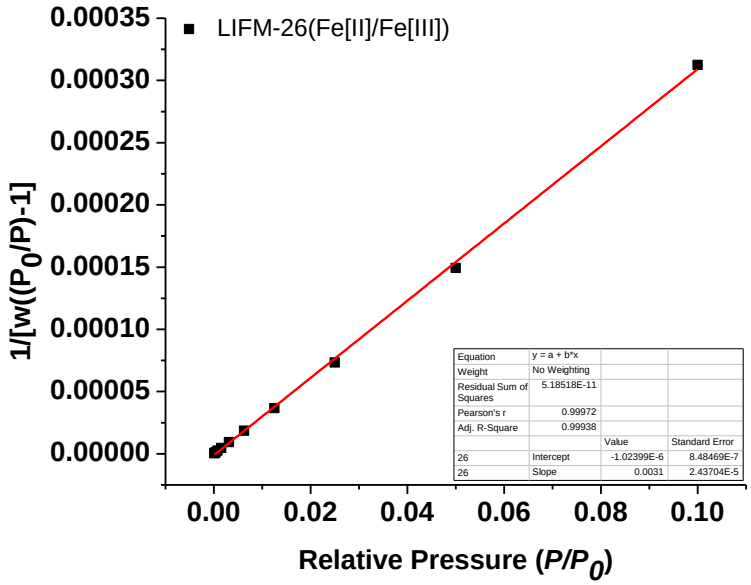

Figure S13. Plot of the linear region on the N_2 isotherm of LIFM-26(Fe[II]/Fe[III]) for the BET equation.

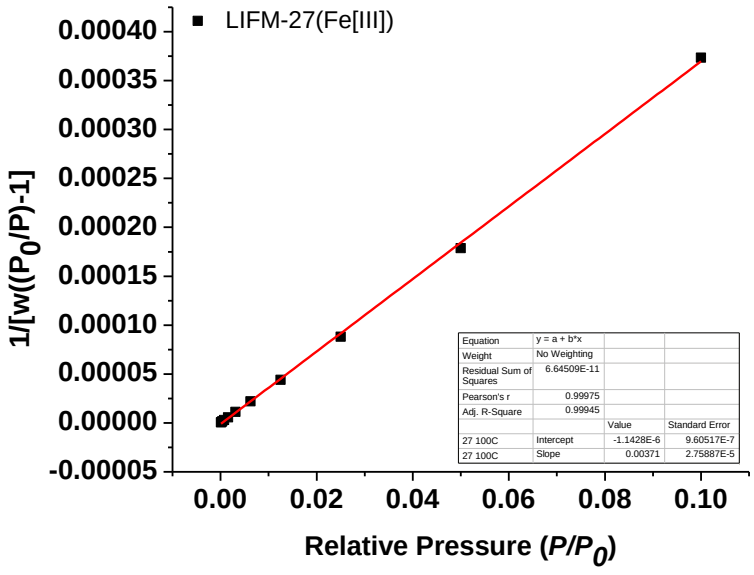

Figure S14. Plot of the linear region on the N_2 isotherm of LIFM-27(Fe[III]) for the BET equation.

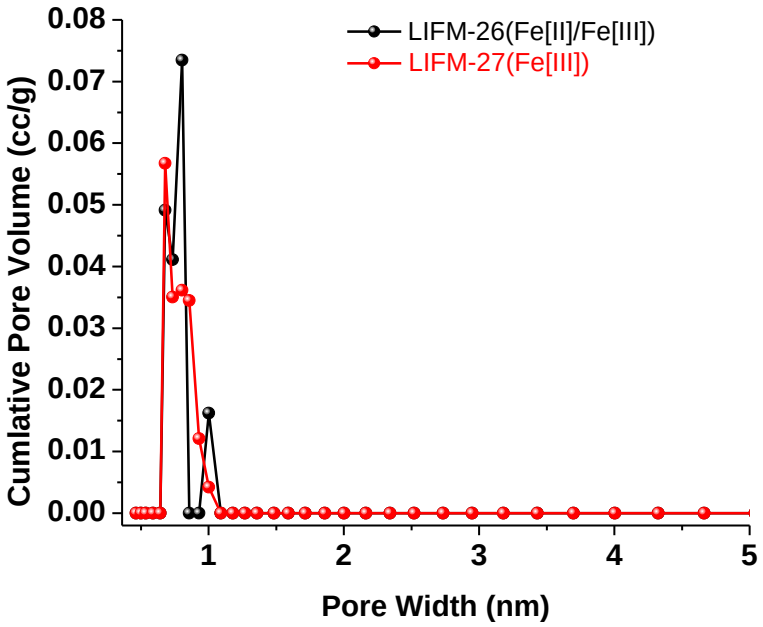

Figure S15. Pore size distribution of LIFM-26(Fe[II]/Fe[III]) and LIFM-27(Fe[III]) calculated by DFT analysis.

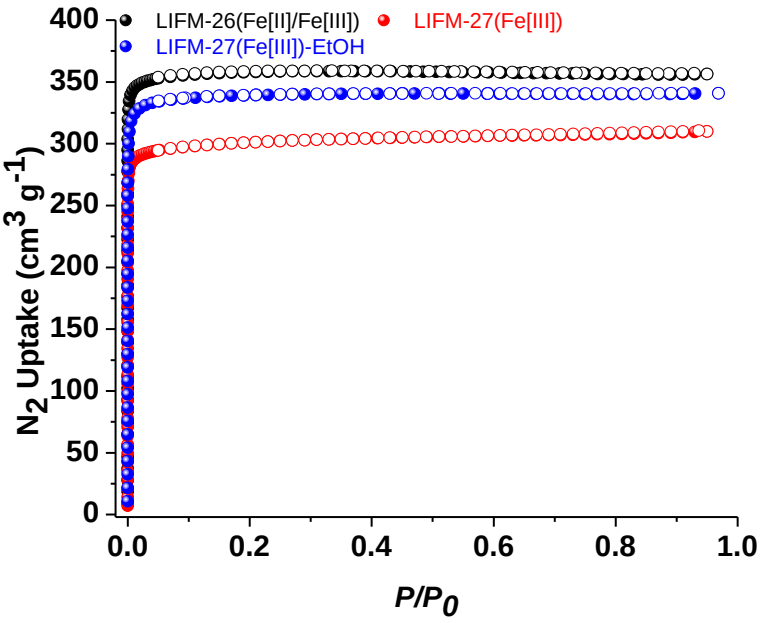

Figure S16. The N_2 (77 K) adsorption isotherms of LIFM-26(Fe[II]/Fe[III]) transformed from LIFM-27(Fe[III]).

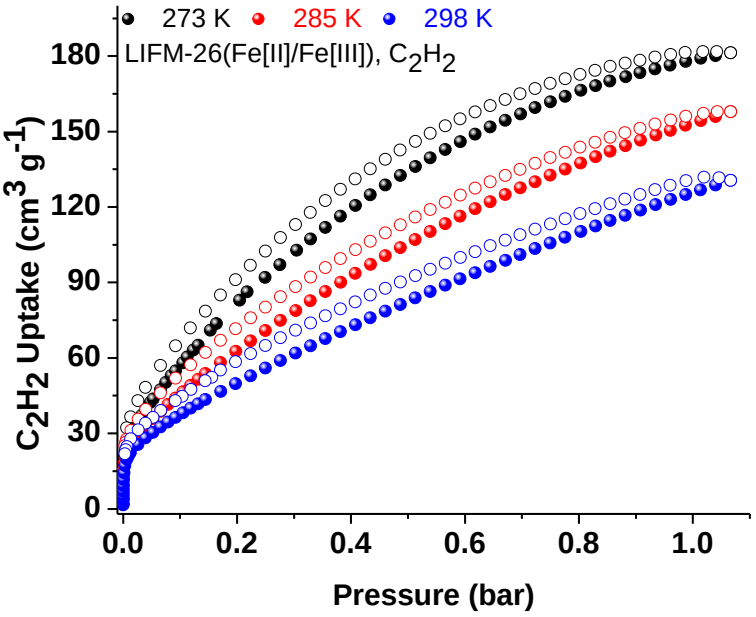

Figure S17. The C_2H_2 adsorption isotherms of LIFM-26(Fe[II]/Fe[III]) at 273 K, 285 K and 298 K.

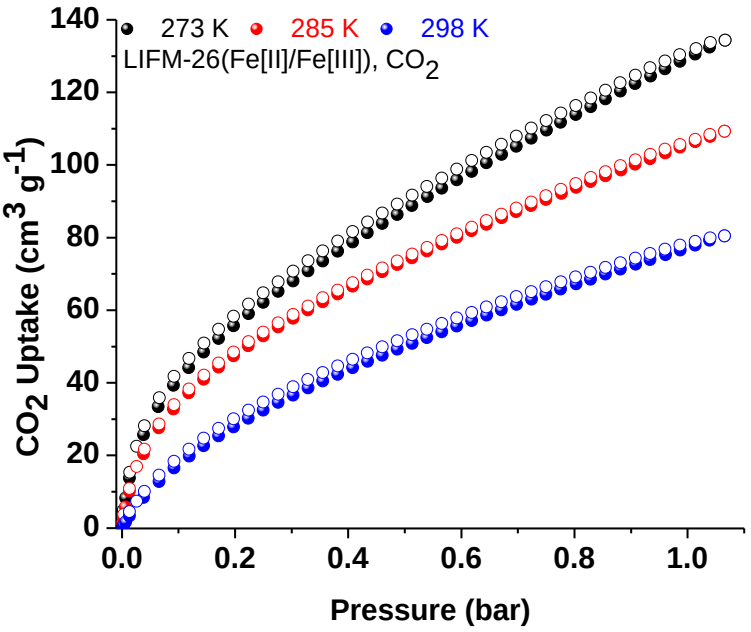

Figure S18. The CO_2 adsorption isotherms of LIFM-26(Fe[II]/Fe[III]) at 273 K, 285 K and 298 K.

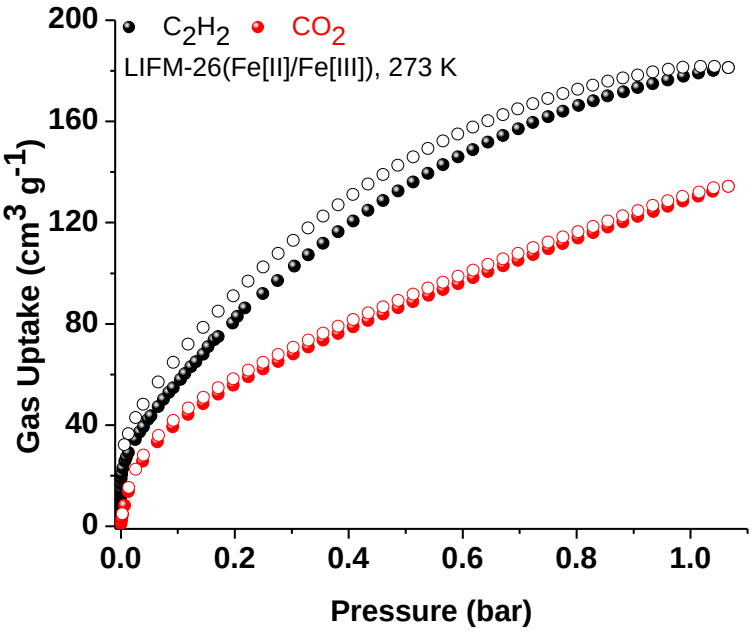

Figure S19. The C_2H_2 and CO_2 adsorption isotherms of LIFM-26(Fe[II]/Fe[III]) at 273 K.

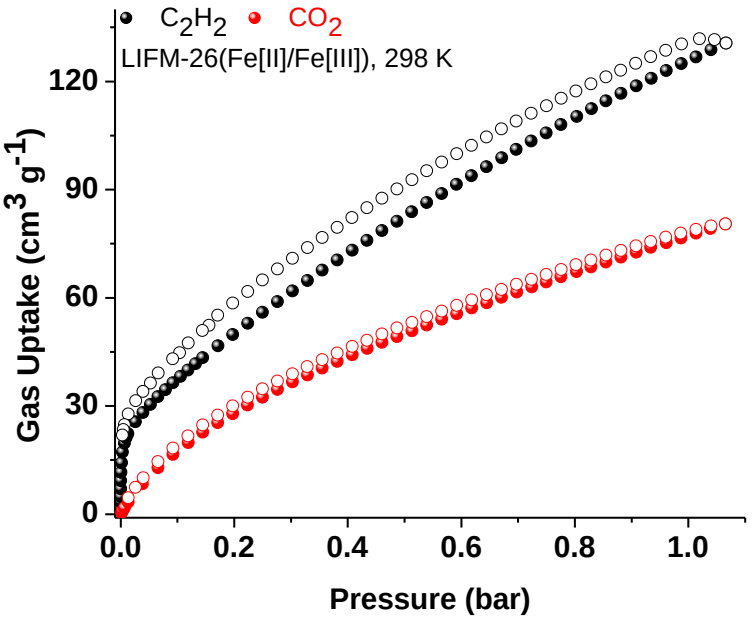

Figure S20. The C_2H_2 and CO_2 adsorption isotherms of LIFM-26(Fe[II]/Fe[III]) at 298 K.

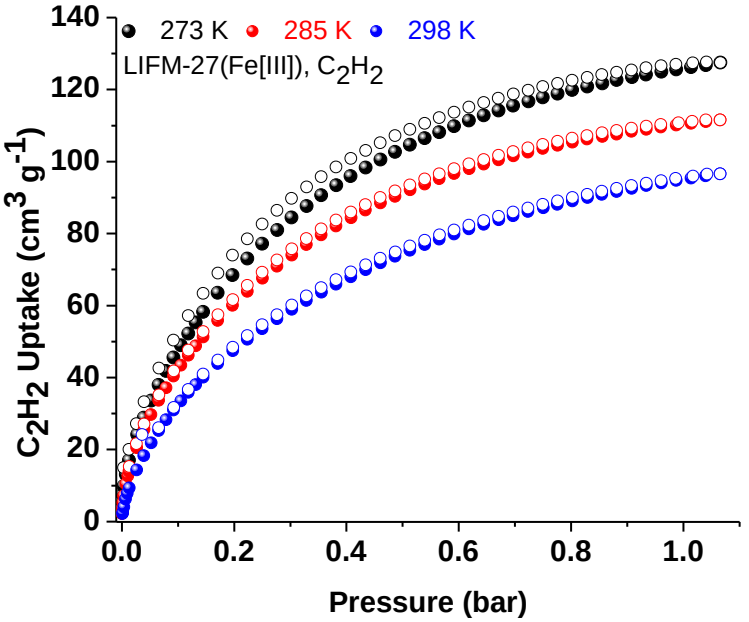

Figure S21. The C_2H_2 adsorption isotherms of LIFM-27(Fe[III]) at 273 K, 285 K and 298 K.

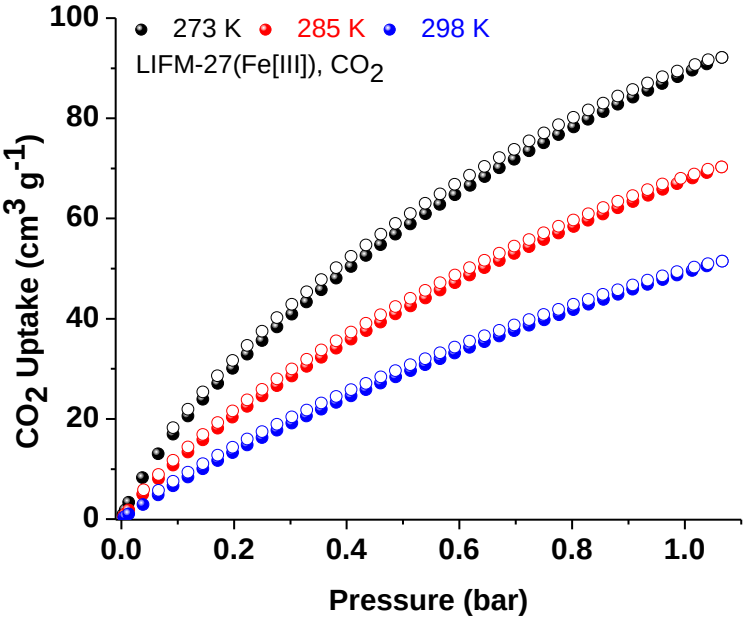

Figure S22. The CO_2 adsorption isotherms of LIFM-27(Fe[III]) at 273 K, 285 K and 298 K.

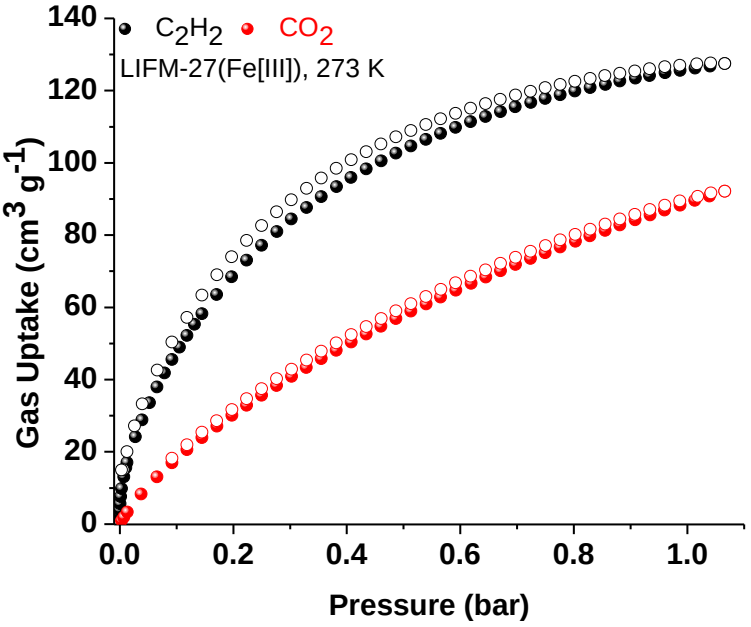

Figure S23. The C_2H_2 and CO_2 adsorption isotherms of LIFM-27(Fe[III]) at 273 K.

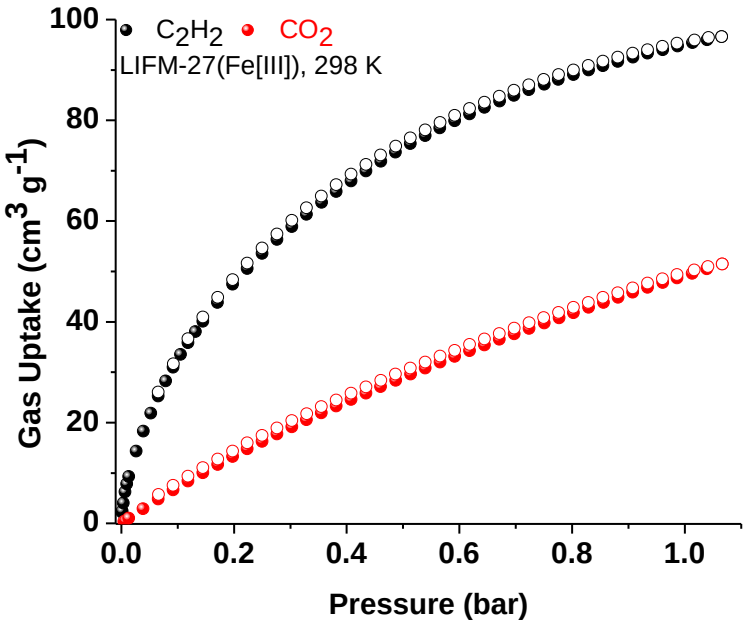

Figure S24. The C_2H_2 and CO_2 adsorption isotherms of LIFM-27(Fe[III]) at 298 K.

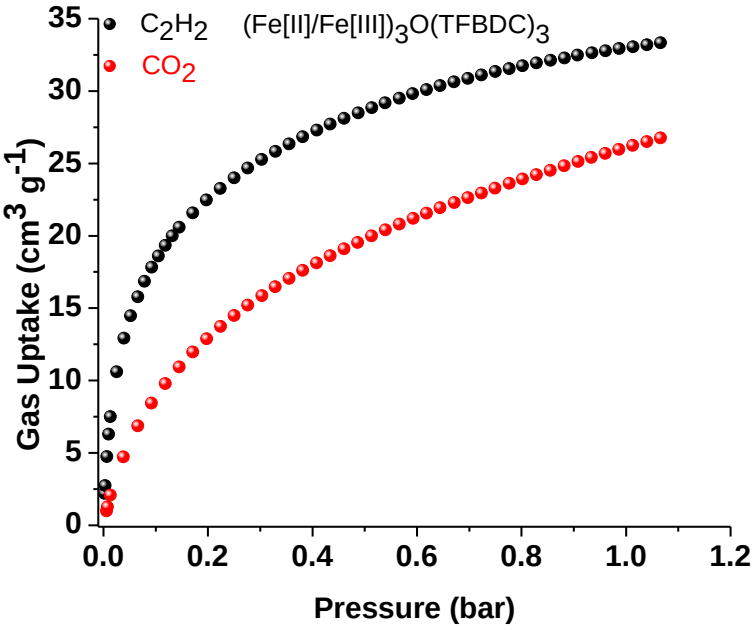

Figure S25. The C_2H_2 and CO_2 adsorption isotherms of $(Fe[II]/Fe[III])_3O(TFBDC)_3$ at 273 K.

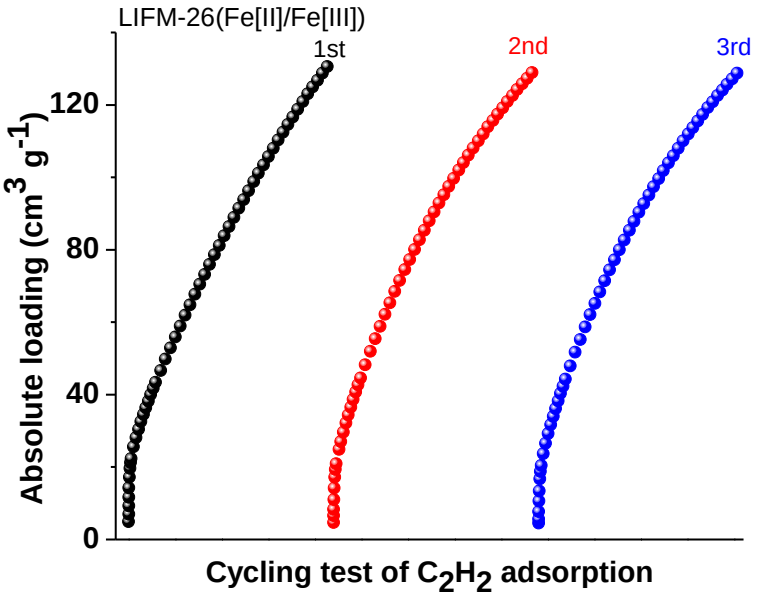

Figure S26. Continuous C_2H_2 adsorption measurements of LIFM-26(Fe[II]/Fe[III]) at 298 K.

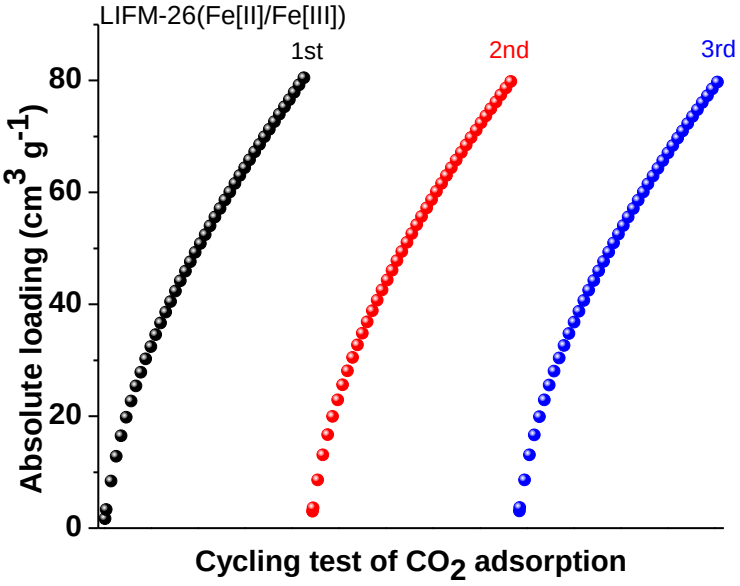

Figure S27. Continuous CO_2 adsorption measurements of LIFM-26(Fe[II]/Fe[III]) at 298 K.

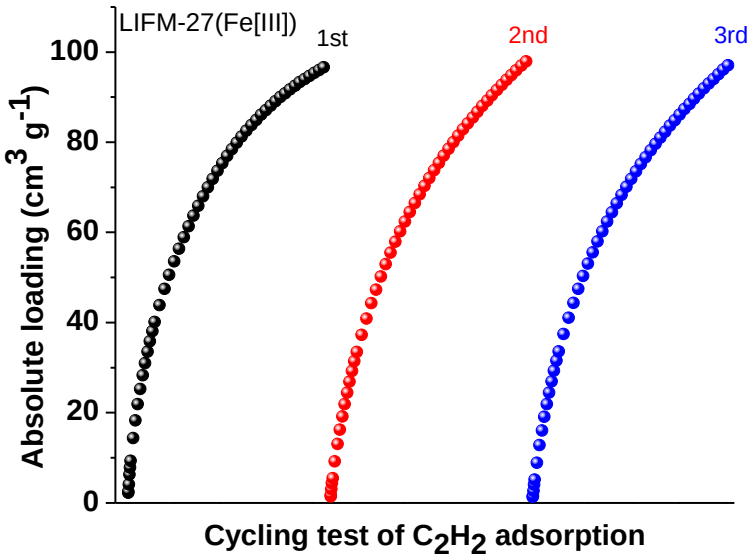

Figure S28. Continuous C_2H_2 adsorption measurements of LIFM-27(Fe[III]) at 298 K.

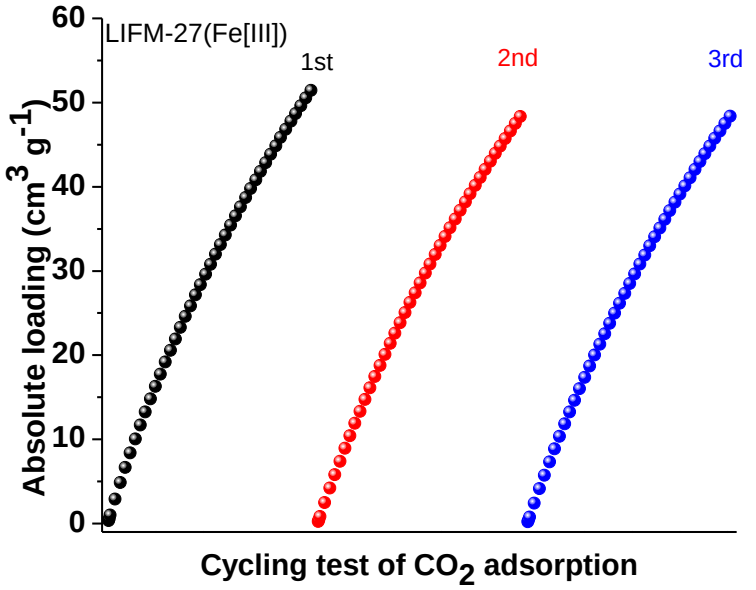

Figure S29. Continuous CO_2 adsorption measurements of LIFM-27(Fe[III]) at 298 K.

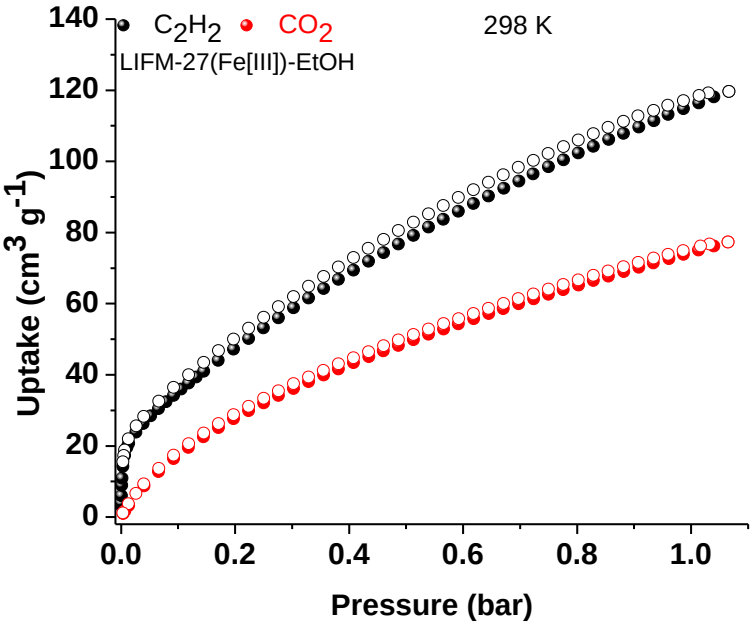

Figure S30. The C_2H_2 and CO_2 adsorption isotherms of LIFM-27(Fe[III])-EtOH treated with EtOH at 298 K.

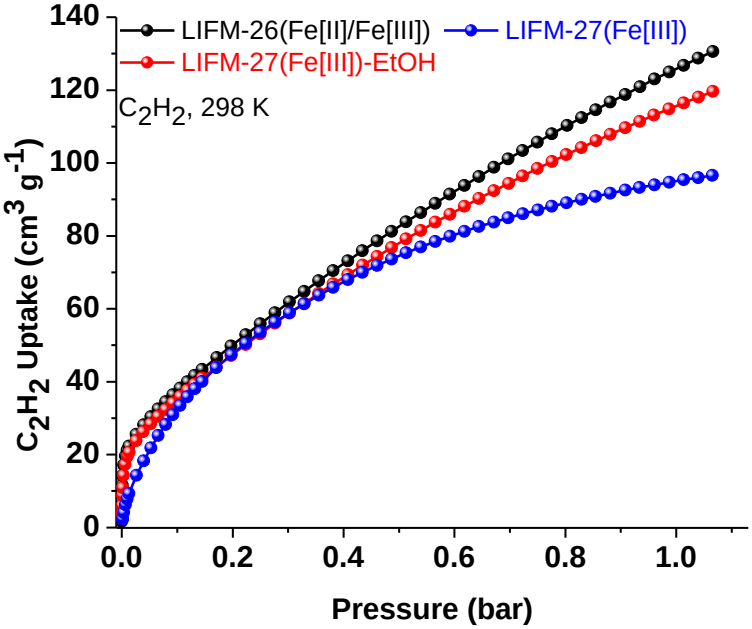

Figure S31. The C_2H_2 adsorption isotherms of LIFM-26(Fe[II]/Fe[III]), LIFM-27(Fe[III]), and LIFM-27(Fe[III])-EtOH at 298 K.

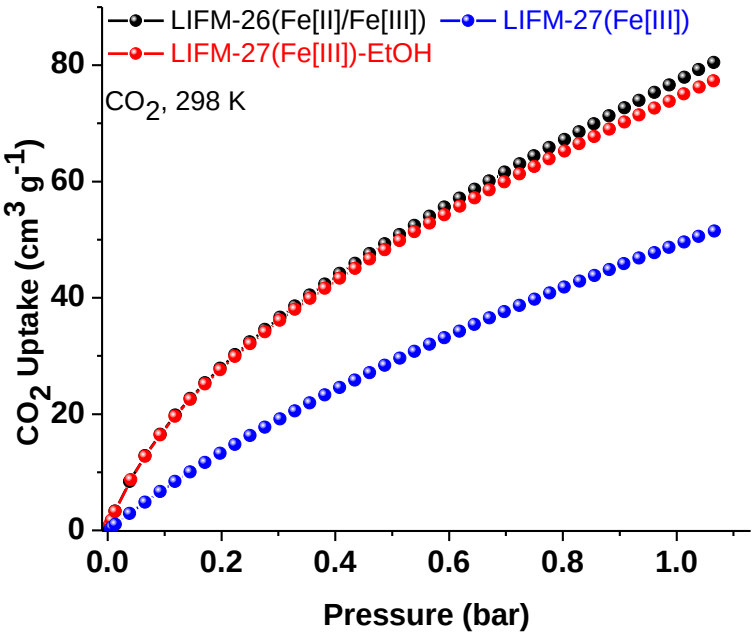

Figure S32. The CO_2 adsorption isotherms of LIFM-26(Fe[II]/Fe[III]), LIFM-27(Fe[III]), and LIFM-27(Fe[III])-EtOH at 298 K.

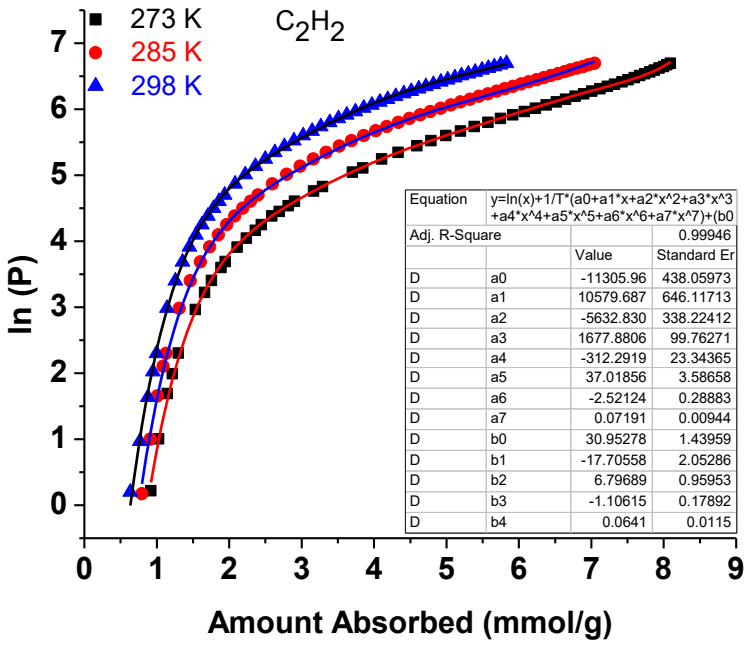

Equation	y=ln(x)+1/T*(a0+a1*x+a2*x^2+a3*x^3 +a4*x^4+a5*x^5+a6*x^6+a7*x^7)+(b0		
Adj. R-Square			0.99946
		Value	Standard Er
D	a0	-11305.96	438.05973
D	a1	10579.687	646.11713
D	a2	-5632.830	338.22412
D	a3	1677.8806	99.76271
D	a4	-312.2919	23.34365
D	a5	37.01856	3.58658
D	a6	-2.52124	0.28883
D	a7	0.07191	0.00944
D	b0	30.95278	1.43959
D	b1	-17.70558	2.05286
D	b2	6.79689	0.95953
D	b3	-1.10615	0.17892
D	b4	0.0641	0.0115

Figure S33. C_2H_2 fitting (lines) of the adsorption isotherms (points) of LIFM-26(Fe[II]/Fe[III]) measured at 273, 285 and 298 K.

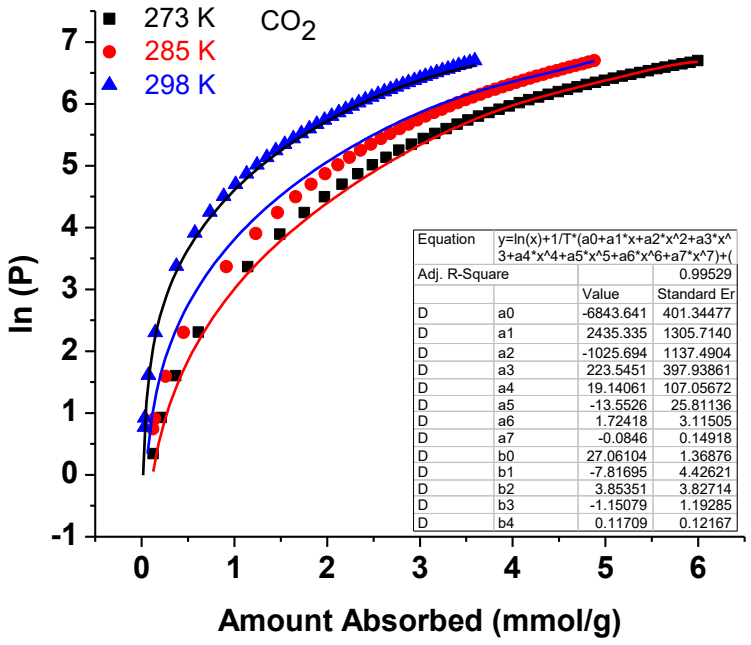

Figure S34. CO_2 fitting (lines) of the adsorption isotherms (points) of LIFM-26(Fe[II]/Fe[III]) measured at 273, 285 and 298 K.

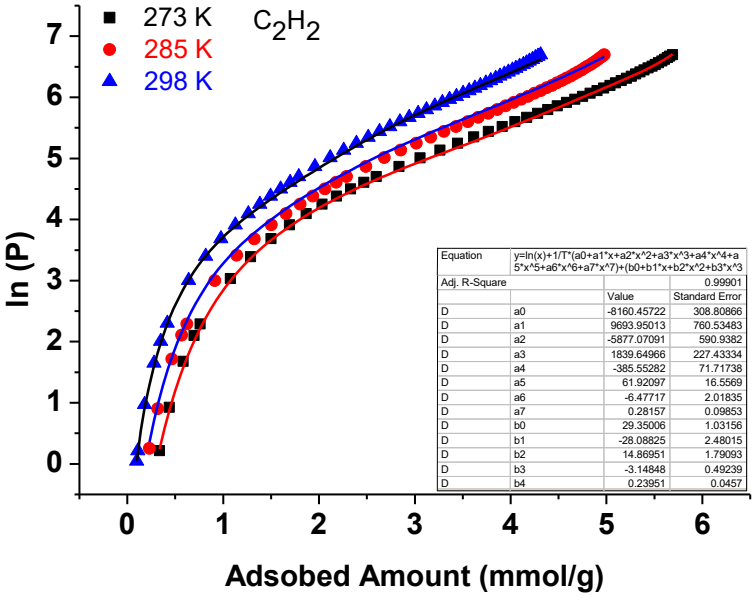

Figure S35. C_2H_2 fitting (lines) of the adsorption isotherms (points) of LIFM-27(Fe[III]) measured at 273, 285 and 298 K.

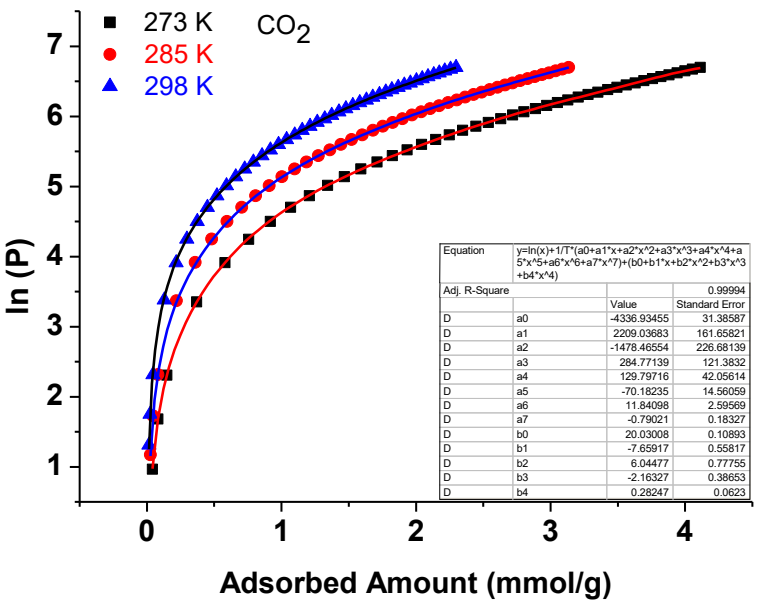

Figure S36. CO_2 fitting (lines) of the adsorption isotherms (points) of LIFM-27(Fe[III]) measured at 273, 285 and 298 K.

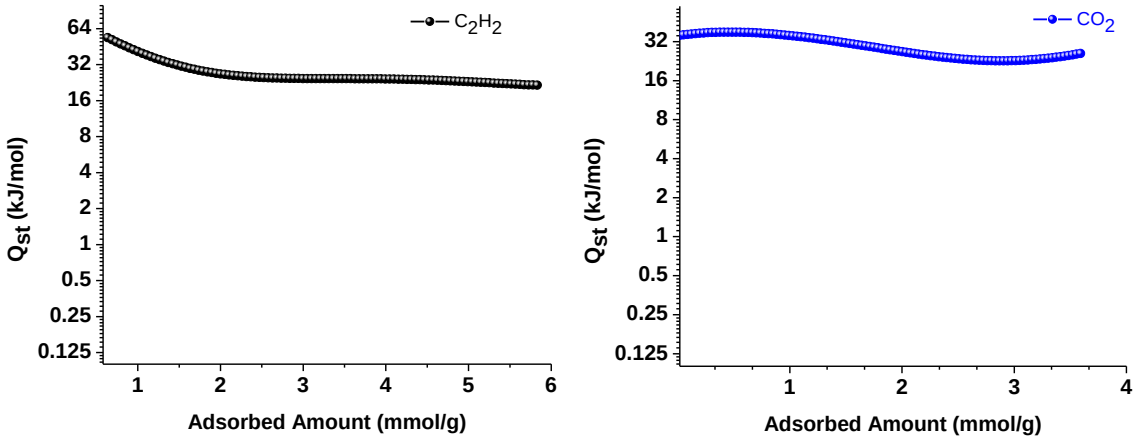

Figure S37. C_2H_2 and CO_2 isosteric heat of adsorption in LIFM-26(Fe[II]/Fe[III]) as a function of surface coverage.

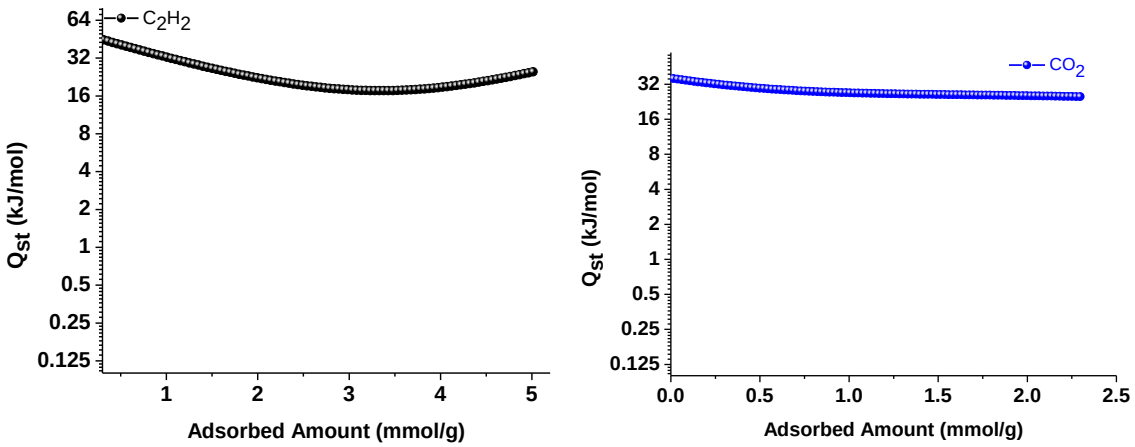

Figure S38. C_2H_2 and CO_2 isosteric heat of adsorption in LIFM-27(Fe[III]) as a function of surface coverage.

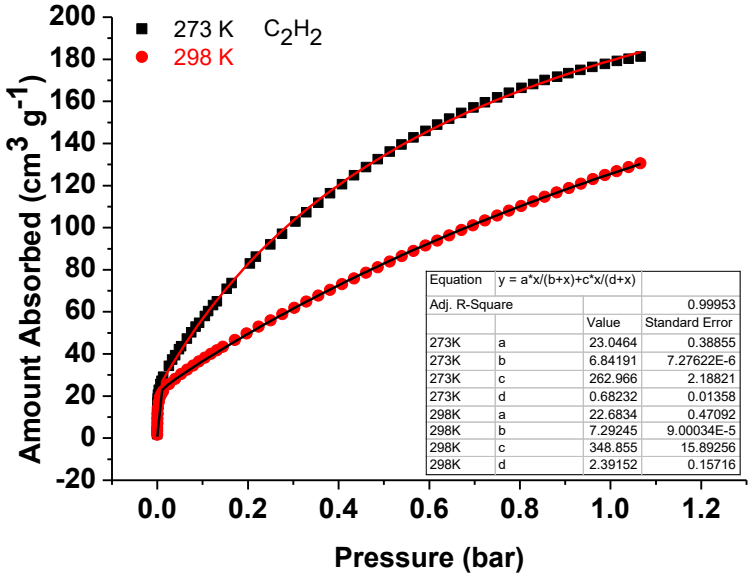

Figure S39. C_2H_2 adsorption isotherms of LIFM-26(Fe[II]/Fe[III]) with fitting by LF model.

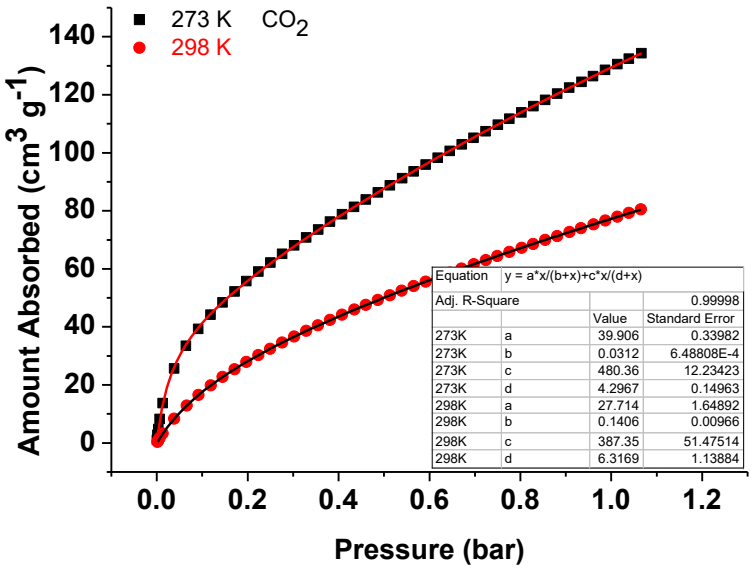

Figure S40. CO_2 adsorption isotherms of LIFM-26(Fe[II]/Fe[III]) with fitting by LF model.

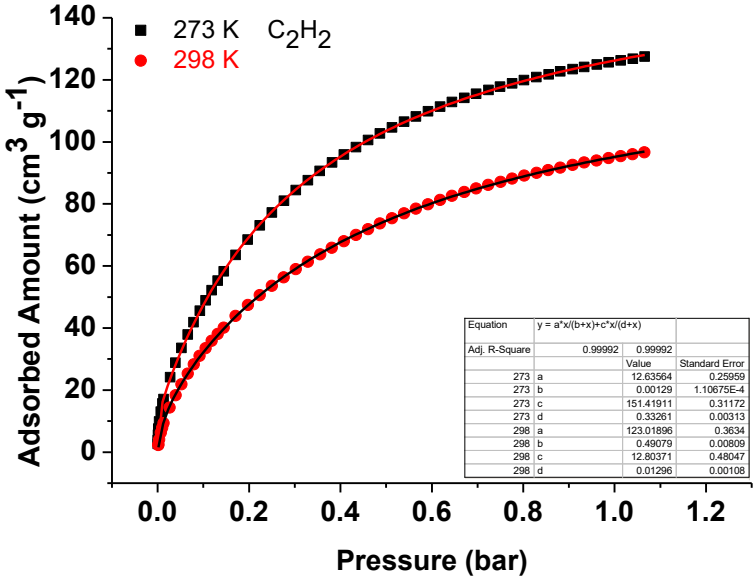

Figure S41. C_2H_2 adsorption isotherms of LIFM-27(Fe[III]) with fitting by LF model.

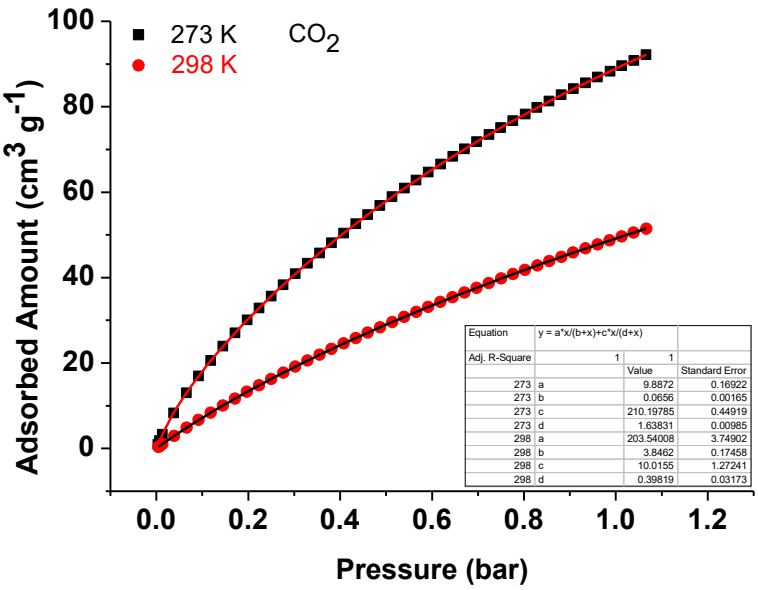

Figure S42. CO_2 adsorption isotherms of LIFM-27(Fe[III]) with fitting by LF model.

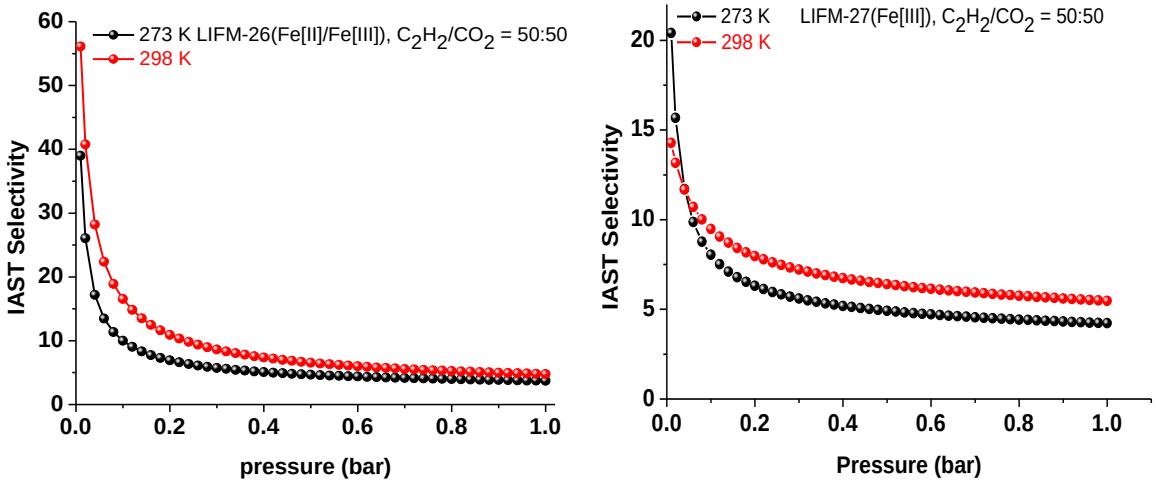

Figure S43. IAST calculative selectivity of C_2H_2/CO_2 (50:50) on LIFM-26(Fe[II]/Fe[III]) and LIFM-27(Fe[III]) at 273 and 298 K.

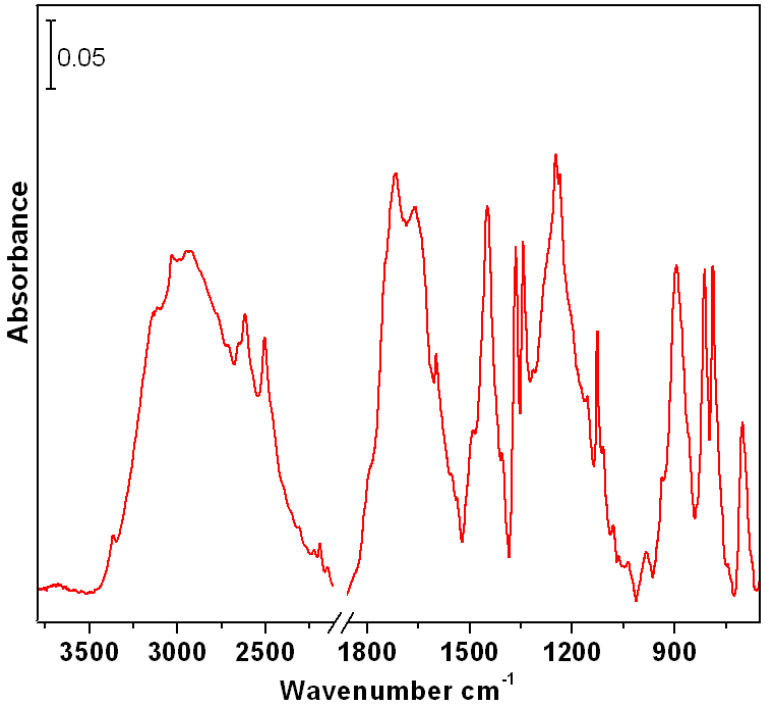

Figure S44. IR spectrum of **TCDC** (referenced to blank KBr pellet).

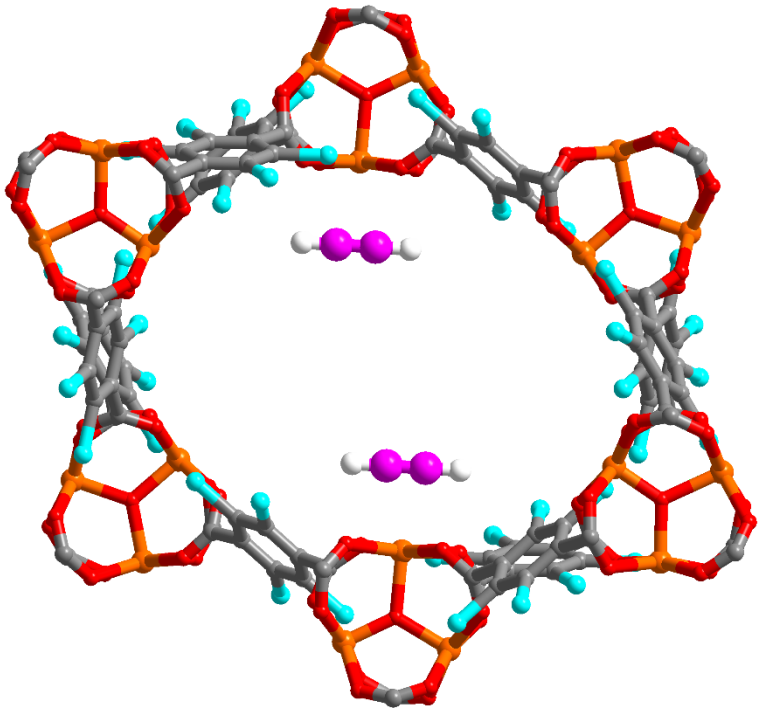

Figure S45. The packing diagram of C_2H_2 in the binding site of LIFM-26(Fe[II]/Fe[III]) observed by the molecular simulation.

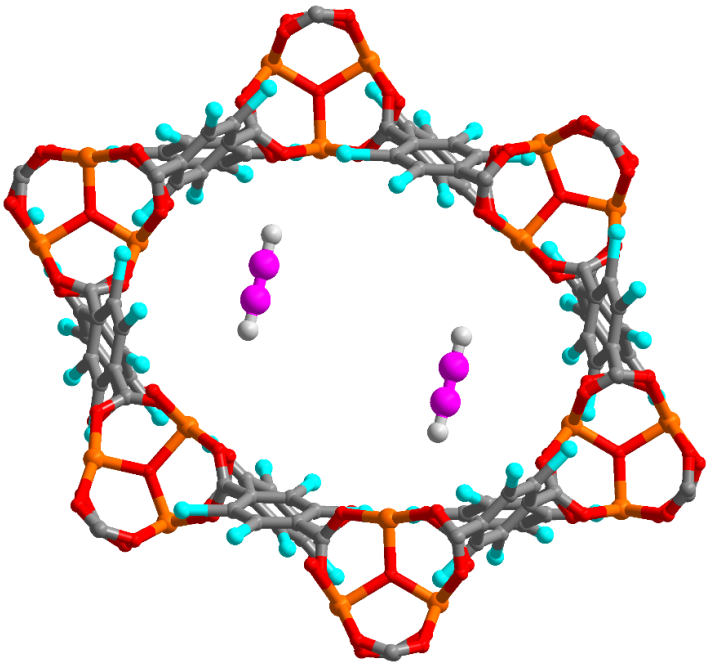

Figure S46. The packing diagram of C_2H_2 in the binding site of LIFM-27(Fe[III]) observed by the molecular simulation.

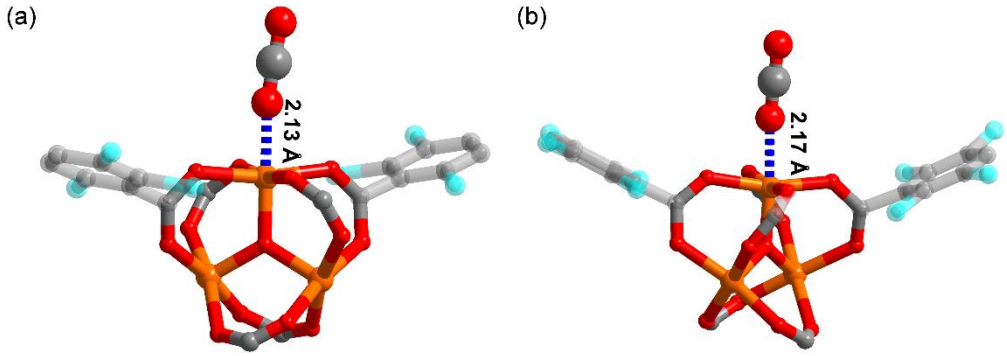

Figure S47. The preferential CO_2 binding sites in LIFM-26(Fe[II]/Fe[III]) (a) and LIFM-27(Fe[III]) (b) observed by model studies.

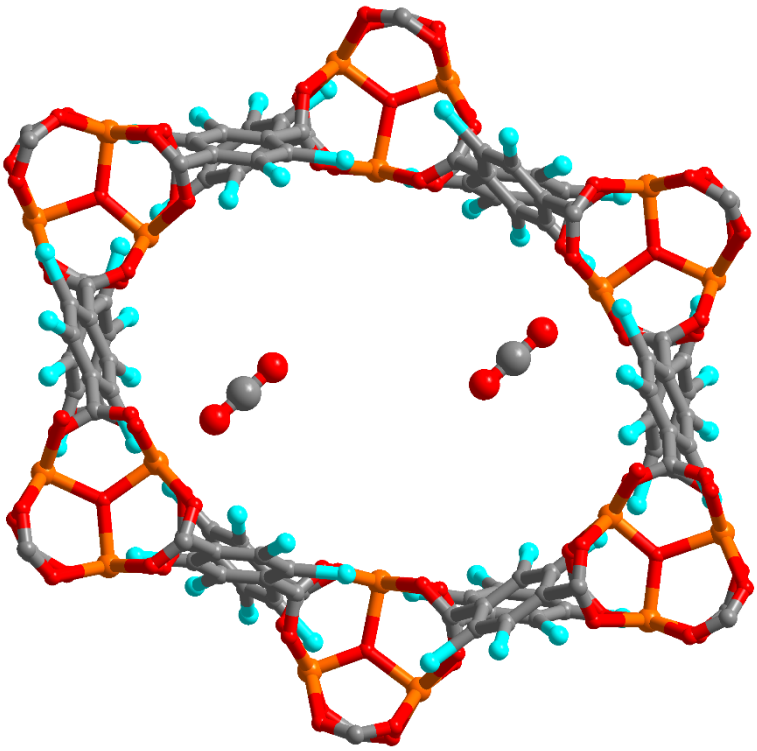

Figure S48. The packing diagram of CO_2 in the binding site of LIFM-26(Fe[II]/Fe[III]) observed by the molecular simulation.

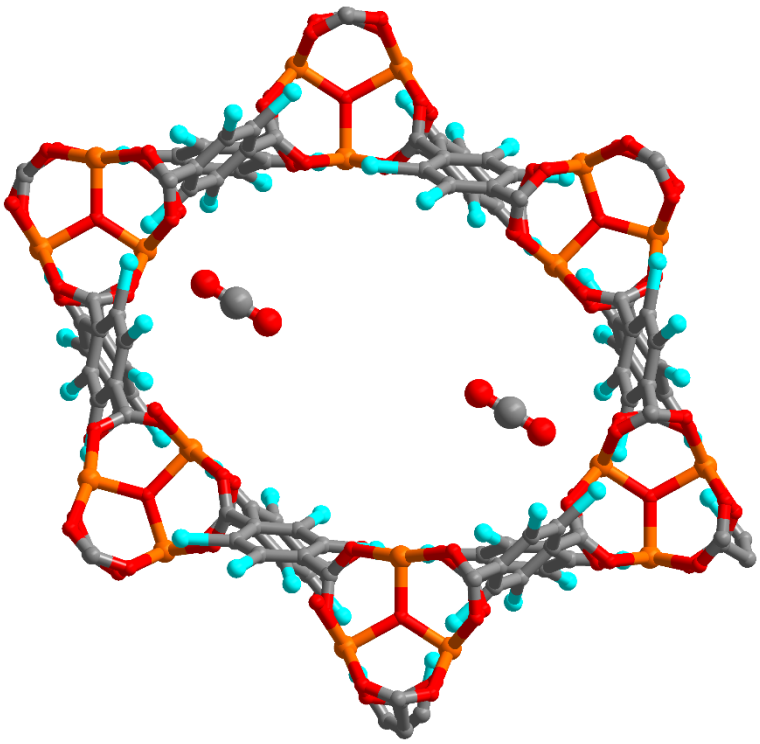

Figure S49. The packing diagram of CO_2 in the binding site of LIFM-27(Fe[III]) observed by the molecular simulation.

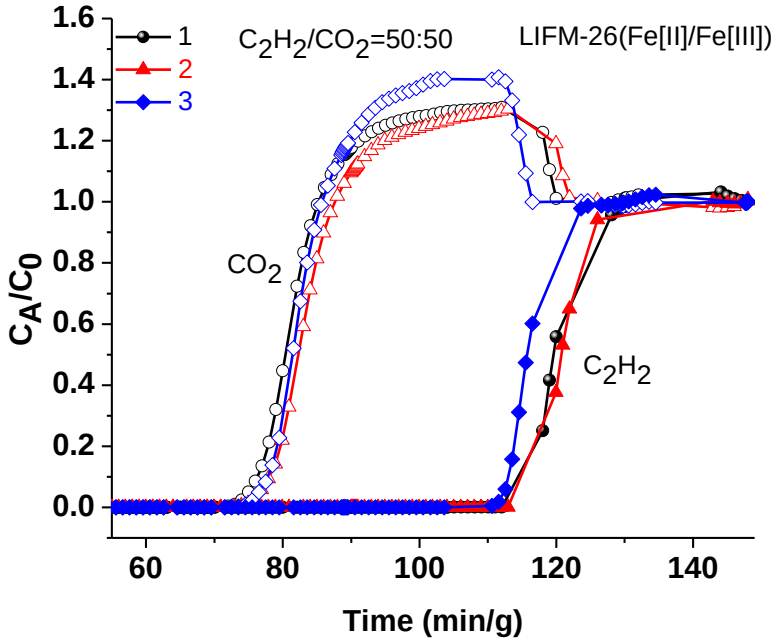

Figure S50. Continuous experimental breakthrough curves of LIFM-26(Fe[II]/Fe[III]) for the 50:50 C_2H_2/CO_2 mixture at 298 K and 1 bar with a constant flow rate of 1.0 mL min^{-1}.

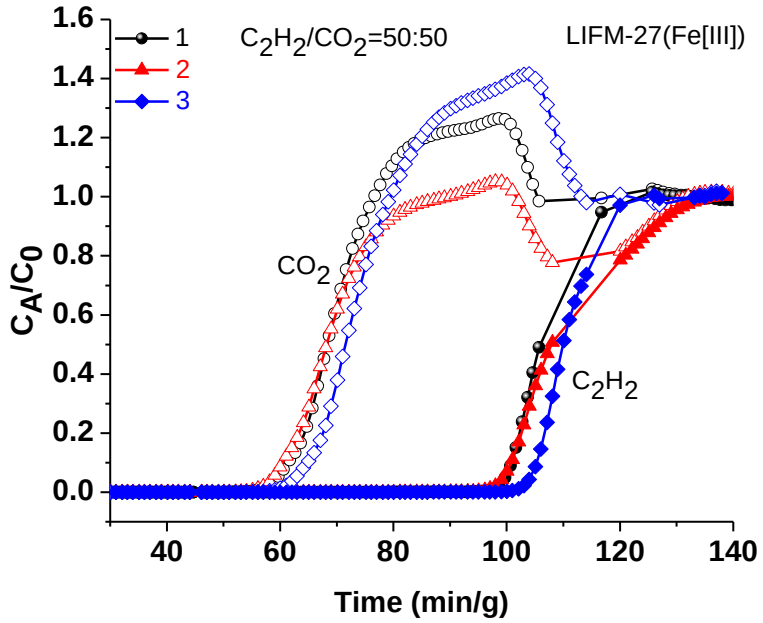

Figure S51. Continuous experimental breakthrough curves of LIFM-27(Fe[III]) for the 50:50 C_2H_2/CO_2 mixture at 298 K and 1 bar with a constant flow rate of 1.0 mL min^{-1}.

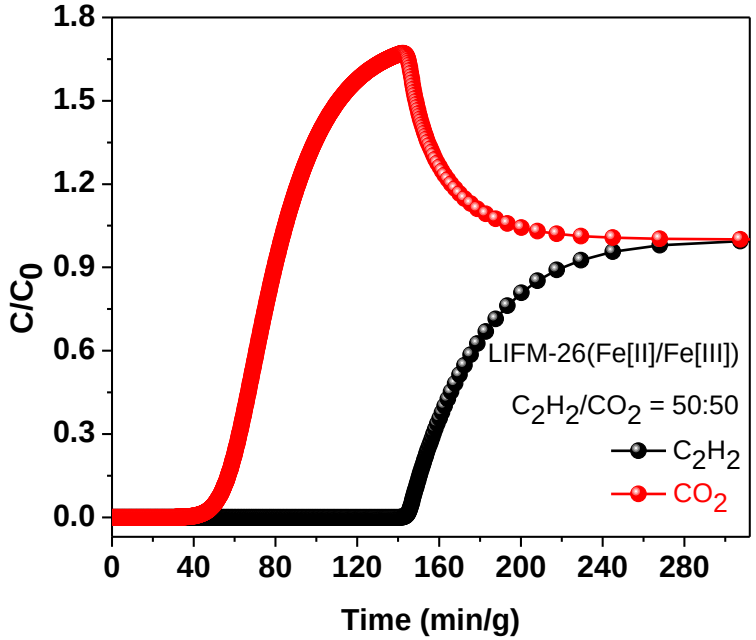

Figure S52. Simulated breakthrough curves of LIFM-26(Fe[II]/Fe[III]) for the 50:50 C_2H_2/CO_2 mixture at 298 K and 1 bar with a constant flow rate of 1.0 mL min^{-1}.

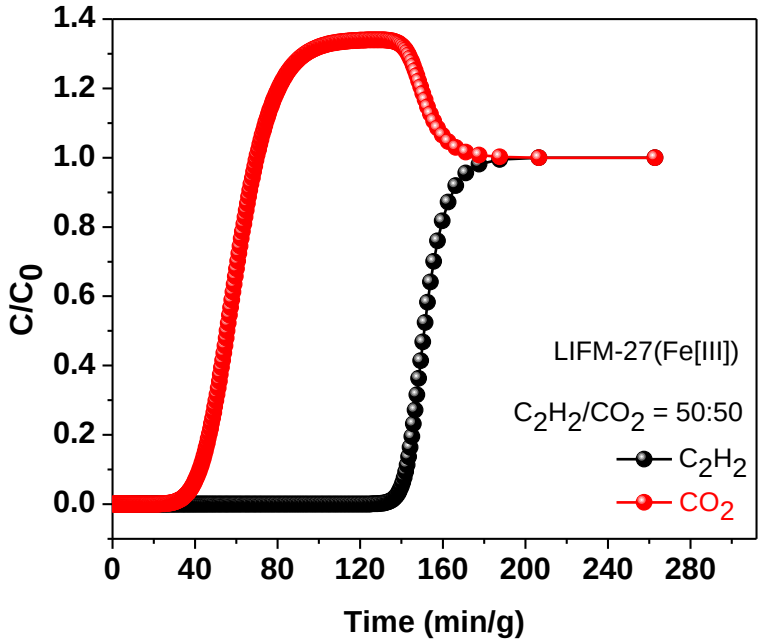

Figure S53. Simulated breakthrough curves of LIFM-27(Fe[III]) for the 50:50 C_2H_2/CO_2 mixture at 298 K and 1 bar with a constant flow rate of 1.0 mL min^{-1}.

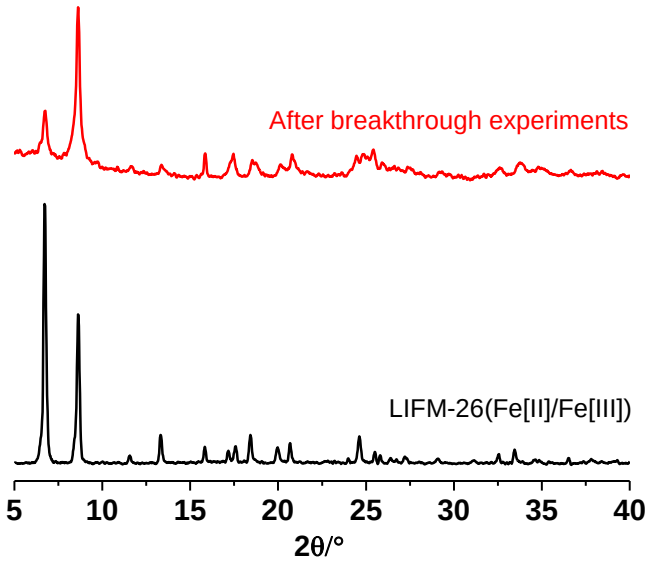

Figure S54. The PXRD patterns of LIFM-26(Fe[II]/Fe[III]) after continuous breakthrough experiments.

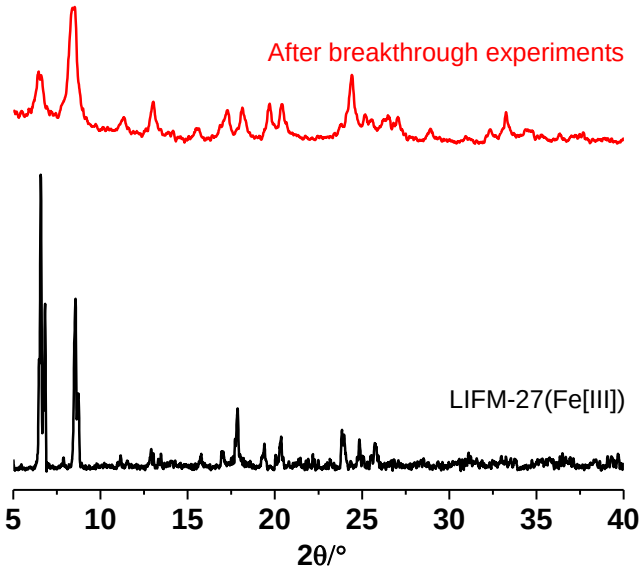

Figure S55. The PXRD patterns of LIFM-27(Fe[III]) after continuous breakthrough experiments.

Table S1. Crystallographic data for LIFM-27(Fe[III])

Compound	**LIFM-27(Fe[III])**
CCDC No.	2114493
Formula	$C_{24}Cl_{12}Fe_3O_{16}$
Formula Weight	1137.19
Shape / Color	Block/ Dark red
Crystal System	Orthorhombic
Space Group	$P2_1/n$
T (K)	150(2)
a (Å)	15.8943(5)
b (Å)	25.2728(9)
c (Å)	16.5535(4)
α / β / γ (°)	90 / 90 / 90
V (Å^3)	6649.5(4)
Z	4
D_{calc} (g/cm^3)	1.136
μ (mm^{-1})	9.980
F (000)	2216.0
Completeness to theta	96.8 %
R_1	0.0890
wR_2	0.2557
GOF	1.060

Table S2. The Mössbauer parameters of LIFM-26(Fe[II]/Fe[III]), LIFM-27(Fe[III]) and LIFM-27(Fe[III])-EtOH derived from the fittings

Component	δ (mm/s)	Q_s (mm/s)	FWHM (mm/s)	Area (%)
LIFM-26(Fe[II]/Fe[III])				
D2	0.78 ± 0.01	---	0.38 ± 0.01	52.4
D3	0.31 ± 0.01	0.56 ± 0.01	0.50 ± 0.01	47.6
LIFM-27(Fe[III])				
D2	0.44 ± 0.01	0.75 ± 0.01	0.49 ± 0.01	100.0
LIFM-27(Fe[III])-EtOH				
D2	0.46 ± 0.01	---	0.56 ± 0.01	67.7
D3	0.22 ± 0.01	0.87 ± 0.01	0.27 ± 0.01	32.3

Table S3. Summary of porosity parameters of LIFM-26(Fe[II]/Fe[III]), LIFM-27(Fe[III]), and (Fe[II]/Fe[III])$_3$O(TFBDC)$_3$(H$_2$O)$_3$

Structure	S_{BET} (m^2 g^{-1})	Total Pore Volume (cc/g)	Pore Size by DFT (Å)
LIFM-26(Fe[II]/Fe[III])	1403	0.55	6.8, 8.0, 10.1
LIFM-27(Fe[III])	1174	0.48	6.8, 8.0
(Fe[II]/Fe[III])$_3$O(TFBDC)$_3$	36	0.026	---

Table S4. Summary of porosity parameters of LIFM-(Fe[II]/Fe[III]) transformed from LIFM-27(Fe[III]).

Structure	S_{BET} (m^2 g^{-1})	Total Pore Volume (cc/g)	Pore Size by DFT (Å)
LIFM-27(Fe[III])-EtOH	1330	0.53	6.8, 8.0, 10.0

Table S5. Comparison of C_2H_2/CO_2 separation performances for some representative MOFs under ambient condition

Materials	C_2H_2 uptake ($cm^3\ g^{-1}$)	CO_2 uptake ($cm^3\ g^{-1}$)	IAST selectivity (C_2H_2/CO_2)	Q_{st} (kJ mol^{-1})		Ref
				C_2H_2	CO_2	
LIFM-26(Fe[II]/[III])	131	80	4.8	53.8	37.8	This work
LIFM-27(Fe[III])	97	51	5.5	44.6	35.8	This work
FJI-H8-Me	229	106	5.6	33.7	21.8	1
FJI-H8	224	---	---	32.0	---	2
FJI-H8-Et	217	102	5.7	29.4	22.7	1
FJI-H8-^{n}Pr	179	92	6.0	29.0	22.6	1
FJI-H8-^{i}Pr	174	90	5.3	28.6	21.7	1
MIL-160	191	90	10	31.8	26.9	3
SIFSIX-Cu-TPA	185	107	5.3	39.1	25.7	4
SNNU-45	134	97.4	4.5	40	27.1	5
ZJU-280a	106	71	18.1	50.6	38.8	6
FeNi-M'MOF	96	61	24	27	24.5	7
ZJU-74a	85.7	66.3	36.5	45	30	8
BSF-3	80.4	47.3	16.3	42.7	22.4	9
ZJUT-2a	76	49	8.5	41.5	35.5	10
JCM-1	75	38	13.7	36.7	33.3	11
JNU-1	64	50.5	3.6	13	24	12
CuI@UiO-66-(COOH)2	52	20	185	74.5	28.9	13
ATC-Cu	112	90	53.6	79.1	---	14
NKMOF-1-Ni	61.0	51.1	22	60.3	40.9	15
HOF-3a	47	21	21.5	2.4	---	16
DICRO-4-Ni-i	43	23	13.9	37.7	33.9	17
JCM-1	75	38	13.7	36.9	33.4	11

UTSA-74a	108.2	70.9	9	31	25	18
SIFSIX-3-Ni	73.9	60.5	7.7	36.7	50.9	19
TIFSIX-2-Cu-i	91.8	96.3	6.5	46.3	35.8	19
FJU-90a	180	103	4.3	25.1	20.7	20
JNU-1	61.7	50.6	3.6	13	---	21
Zn-MOF-74a	78.2	76.1	2.8	43.8	31.7	22

Table S6. Calculated averaged total potential energies (in kJ mol^{-1}) for a single C_2H_2 and CO_2 molecules, individually, positioned at their global minimum in LIFM-26(Fe[II]/Fe[III]) and LIFM-27(Fe[III]) as determined from CMC simulations at 20 K/1.0 atm

Structure	MOF-C_2H_2 Energy (kJ mol^{-1})	MOF-CO_2 Energy (kJ mol^{-1})
LIFM-26(Fe[II]/Fe[III])	-49.7	–38.5
LIFM-27(Fe[III])	-45.6	–37.6

Supplemental Experimental Procedures

Materials and Instrumentation

All the reagents and solvents were purchased from commercial sources and directly utilized without further purification. Tetrachloroterephthalic acid (**TCDC**) was purchased from Aladdin. Tetrafluoroterephthalic acid (**TFBDC**) were purchased from Fisher Scientific. Solid-state IR spectra were recorded using Nicolet/Nexus-670 FT-IR spectrometer in the region of 4000-400 cm^{-1} using KBr pellets. Single-crystal X-ray diffraction data were collected on a Rigaku Oxford SuperNova X-RAY diffractometer system equipped with a Cu sealed tube (λ = 1.54178) at 50 kV and 0.80 mA. Powder X-ray diffraction (PXRD) was carried out with a Rigaku SmartLab diffractometer (Bragg-Brentano geometry, Cu Kα1 radiation, λ = 1.54056 Å). Thermogravimetric analyses (TGA) were performed on a NETZSCH TG209 system in nitrogen and under 1 atm of pressure at a heating rate of 10 °C min^{-1}. Gas adsorption isotherms for pressures in the range of 0-1.0 bar were obtained by a volumetric method using Micromeritics ASAP 2020 physisorption analyzer. Gas adsorption measurements were performed using ultra-high purity N_2, CO_2, C_2H_2 and C_2H_4 gas.

MOF Synthesis

Synthesis of LIFM-26(Fe[II]/Fe[III])

LIFM-26 was prepared using a literature procedure.[23]

Synthesis of LIFM-27(Fe[III])

TCDC (1 g) and $FeCl_2$•$4H_2O$ (4 g) were dissolved in the mixture of 190 mL *N*,*N*'-dimethylformamide (DMF) and 110 mL H_2O in a 500 mL glass flask, which is put into a desiccator with 500 mL n-PrOH and 1.0 mL Et_3N. Dark brown crystals were obtained after about two weeks. The crystals were washed with DMF for 3～5 times, and then stored in 30 mL DMF.

Synthesis of (Fe[II]/Fe[III])$_3$O(TFBDC)$_3$

$(Fe^{II}/Fe^{III})_3O$(**TFBDC**)$_3$ was synthesized according to the documented procedure.[24]

The transformation from LIFM-27(Fe[III]) to LIFM-26(Fe[II]/Fe[III]), denoted as LIFM-27(Fe[III])-EtOH

As-prepared LIFM-27(Fe^{III}) (100 mg) was washed with EtOH (20mL × 3) and then soaked in 20 mL EtOH. The mixture was heated at 75 ^oC for 72 h, during which the solvent was decanted and freshly replenished two times a day. After cooling down to room temperature, the crystals of LIFM-26 were collection by filtration and soaked in EtOH.

Single Crystal X-Ray Crystallography

Single crystal of LIFM-27(Fe[III]) was carefully picked, attached to a glass silk which was inserted in a stainless steel stick, then quickly transferred to a Rigaku Oxford Gemini S Ultra CCD Diffractometer with the Enhance X-ray Source of Cu radiation (λ = 1.54178 Å) using the ω-ϕ scan technique. The structure was solved by direct methods and refined by full-matrix least squares against F^2 using the SHELXL programs.[25] Hydrogen atoms were placed in geometrically calculated positions and included in the refinement process using riding model with isotropic thermal parameters: Uiso(H) = 1.2 Ueq(-CH). Crystal and refinement parameters are listed in Table S1.

Calculations of Adsorption Isosteric Heats:

The isosteric heats of C_2H_2 and CO_2 adsorption for LIFM-26(Fe[II]/Fe[III]) and LIFM-27(Fe[III]) were calculated from the sorption data measured at 273 K, 285 K and 298 K by the virial fitting method, respectively. A virial-type expression (eq. 1) which is composed of parameters a_i and b_i is used. In eq. 1, P is the pressure in torr, N is the adsorbed amount in mmol·g^{-1}, T is the temperature in Kelvin, a_i and b_i are the virial coefficients which are independent of temperature, and m and n are the numbers of coefficients required to adequately describe the isotherms.

$$\ln P = \ln N + \frac{1}{T}\sum_{i=0}^{m} a_i N^i + \sum_{i=0}^{n} b_i N^i \qquad \text{eq. 1}$$

The values of the virial coefficients a_0 through a_m were then applied to calculate the isosteric heat of adsorption (eq 2). In eq. 2, Q_{st} is the coverage-dependent isosteric heat of adsorption and *R* is the universal gas constant.[26]

$$Q_{st} = -R\sum_{i=0}^{m} a_i N^i \qquad \text{eq. 2}$$

C_2H_2/CO_2 Selectivity Calculation via IAST

The experimental isotherm data for pure C_2H_2 and CO_2 (measured at 273 K and 298 K) were fitted using a Langmuir Freundlich (LF) model:

$$q = \frac{a*b*p^{1/n}}{1+b*p^{1/n}} \qquad \text{eq. 3}$$

Where q and p are adsorbed amounts and pressure of component i, respectively.

The adsorption selectivities for binary mixtures of C_2H_6/C_2H_4 defined by

$$S_{i/j} = \frac{x_i}{x_j} * \frac{y_j}{yi} \qquad \text{eq. 4}$$

were calculated using the Ideal Adsorption Solution Theory (IAST) of Myers and Prausnitz.[27] Where x_i is the mole fraction of component i in the adsorbed phase and y_i is the mole fraction of component i in the bulk.

in situ infrared (IR) spectroscopy

In situ IR measurements were performed on a Nicolet 6700 FTIR spectrometer using a liquid N_2-cooled mercury cadmium telluride (MCT-A) detector. The spectrometer is equipped with a vacuum cell which is placed in the main compartment with the sample at the focal point of the infrared beam. The samples (~5 mg) were gently pressed onto KBr pellet and placed into a cell that is connected to a vacuum line for evacuation. The samples were activated by ~5 h evacuation at 150-180 ºC, and then cooled back to room temperature for C_2H_2 gas adsorption measurement.

Modeling Studies

The binding sites for C_2H_2 and CO_2 in LIFM-26(Fe[II]/Fe[III]) and LIFM-27(Fe[III]) were determined through classical molecular simulations. The single X-ray crystallographic structures that were published herein for the respective MOFs were used as a starting point to perform the parametrizations and simulations. Missing H atoms that are part of the bridging OH^- groups were manually inserted where appropriate in both MOFs. These H atoms were then optimized using the Material Studios[28] Forcite module with the lattice parameters of the MOF held constant.

All atoms of LIFM-26(Fe[II]/Fe[III]) and LIFM-27(Fe[III]) were treated with Lennard-Jones (LJ) parameters (ε and σ)[29] and point partial charges in order to model repulsion/dispersion and stationary electrostatic interactions, respectively. The LJ parameters for all aromatic C and H atoms were taken from the Optimized Potentials for Liquid Simulations - All Atom (OPLS-AA) force field,[30] while those for all other atoms were taken from the Universal Force Field (UFF).[31] The partial charges for the unique atoms in LIFM-26(Fe[II]/Fe[III]) and LIFM-27(Fe[III]) were determined through the extended charge equilibration (EQ_{eq}) method.[32]

Simulated annealing (SA) calculations[33] were performed for a single molecule of each adsorbate through a canonical Monte Carlo (CMC) process in the 1 × 1 × 2 supercells of LIFM-26(Fe[II]/Fe[III]) and LIFM-27(Fe[III]). All MOF atoms were kept fixed at their crystallographic positions throughout the simulations. A spherical cut-off distance corresponding to half the shortest supercell dimension length was used for the simulations in both MOFs. C_2H_2 and CO_2 were modeled using electrostatic potentials of the respective adsorbates that were developed previously.[34-36] The total potential energy of the MOF-adsorbate system was calculated through the sum of the repulsion/dispersion and stationary electrostatic energies. These were calculated

using the LJ potential[2] and the Ewald summation technique,[37; 38] respectively. SA calculations for each adsorbate utilized an initial temperature of 500 K, and this temperature was scaled by a factor of 0.99999 after every 10^3 Monte Carlo (MC) steps. The simulations continued until 10^6 MC steps were reached; at this point, the temperature of the system is below 25 K and the adsorbate is already localized in its energy minimum position in the MOF. All simulations were carried out using the Massively Parallel Monte Carlo (MPMC) code.[39; 40]

Next, CMC simulations[41] were performed for a single molecule of C_2H_2 and CO_2, individually, positioned at their global minimum in LIFM-26(Fe[II]/Fe[III]) and LIFM-27(Fe[III]). This was done in order to evaluate the averaged classical potential energy for all three adsorbates about their energy minimum position in the material. The CMC simulations were performed at a temperature of 20 K and a pressure of 1.0 atm. These simulations ran for a total of 10^6 MC steps to ensure reasonable ensemble averages for the total potential energy of the system. The averaged classical potential energies for C_2H_2 and CO_2 localized about their energy minimum position in LIFM-26(Fe[II]/Fe[III]) and LIFM-27(Fe[III]) are presented in Table S6.

Breakthrough separation experiments and procedures

The breakthrough experiments were carried out in a dynamic gas breakthrough set-up.[42] All experiments were conducted using a stainless steel column (3.0 mminner diameter ×120 mm) with silica wool filling the void space. According to the different particle size and density of the sample powder, the weight packed in the column was: 0.470 g for LIFM-26(Fe[II]/Fe[III]), 0.330 g for LIFM-27(Fe[III]). Outlet gas from the column was monitored using gas chromatography (GC-490) with a thermal conductivity detector (TCD) coupled with a FID. The mixed gas flow rate during breakthrough process is 1.0 mL min^{-1} for 50/50 (v/v) C_2H_2/CO_2, respectively. After the breakthrough experiment, the sample was regenerated under N_2 flow.

Transient breakthrough simulations

Transient breakthrough simulations of the adsorption were carried out based on the experimental breakthrough conditions with binary 50/50 C_2H_2/CO_2 mixtures at a total pressure of 100 kPa and 298 K with the total flow rate of 1 mL min^{-1}, using the methodology described in earlier publications.[43-47] In these simulations, intra-crystalline diffusion influences are ignored.

Notation

b: Langmuir-Freundlich constant, Pa^{-v}; q_i: component molar loading of species *i*, mol kg^{-1}; q_{sat}: saturation loading, mol kg^{-1}; p_i: partial pressure of species *i* in mixture, Pa; p_t: total system pressure, Pa; *t*: time, min/g; *T*: absolute temperature, K.

Greek letters

v: Freundlich-exponent, dimensionless.

Supplemental References

1 Di, Z., Liu, C., Pang, J., Chen, C., Hu, F., Yuan, D., Wu, M., and Hong, M. (2021). Cage-Like Porous Materials with Simultaneous High C_2H_2 Storage and Excellent C_2H_2/CO_2 Separation Performance. Angew. Chem. Int. Ed. *60*, 10828-10832.

2 Pang, J., Jiang, F., Wu, M., Liu, C., Su, K., Lu, W., Yuan, D., and Hong, M. (2015). A porous metal-organic framework with ultrahigh acetylene uptake capacity under ambient conditions. Nat. Commun. *6*, 7575-7581.

3 Ye, Y., Xian, S., Cui, H., Tan, K., Gong, L., Liang, B., Pham, T., Pandey, H., Krishna, R., Lan, P.C., Forrest, K.A., Space, B., Thonhauser, T., Li, J., and Ma, S. (2022). Metal-Organic Framework Based Hydrogen-Bonding Nanotrap for Efficient Acetylene Storage and Separation. J. Am. Chem. Soc. *144*, 1681-1689.

4 Li, H., Liu, C., Chen, C., Di, Z., Yuan, D., Pang, J., Wei, W., Wu, M., and Hong, M. (2021). An Unprecedented Pillar-Cage Fluorinated Hybrid Porous Framework with Highly Efficient Acetylene Storage and Separation. Angew. Chem. Int. Ed. *60*, 7547-7552.

5 Li, Y.P., Wang, Y., Xue, Y.Y., Li, H.P., Zhai, Q.G., Li, S.N., Jiang, Y.C., Hu, M.C., and Bu, X. (2019). Ultramicroporous Building Units as a Path to Bi-microporous Metal-Organic Frameworks with High Acetylene Storage and Separation Performance. Angew. Chem. Int. Ed. *58*, 13590-13595.

6 Qian, Q.-L., Gu, X.-W., Pei, J., Wen, H.-M., Wu, H., Zhou, W., Li, B., and Qian, G. (2021). A novel anion-pillared metal-organic framework for highly efficient separation of acetylene from ethylene and carbon dioxide. J. Mater. Chem. A *9*, 9248-9255.

7 Gao, J., Qian, X., Lin, R.B., Krishna, R., Wu, H., Zhou, W., and Chen, B. (2020). Mixed Metal-Organic Framework with Multiple Binding Sites for Efficient C_2H_2/CO_2 Separation. Angew. Chem. Int. Ed. *59*, 4396-4400.

8 Pei, J., Shao, K., Wang, J.X., Wen, H.M., Yang, Y., Cui, Y., Krishna, R., Li, B., and Qian, G. (2020). A Chemically Stable Hofmann-Type Metal-Organic Framework with Sandwich-Like Binding Sites for Benchmark Acetylene Capture. Adv. Mater. *32*, 1908275-1908281.

9 Zhang, Y., Hu, J., Krishna, R., Wang, L., Yang, L., Cui, X., Duttwyler, S., and Xing, H. (2020). Rational Design of Microporous MOFs with Anionic Boron Cluster Functionality and Cooperative Dihydrogen Binding Sites for Highly Selective Capture of Acetylene. Angew. Chem. Int. Ed. *59*, 17664-17669.

10 Wen, H.-M., Liao, C., Li, L., Yang, L., Wang, J., Huang, L., Li, B., Chen, B., and Hu, J. (2019). Reversing C_2H_2-CO_2 adsorption selectivity in an ultramicroporous metal–organic framework platform. Chem. Commun. *55*, 11354-11357.

11 Lee, J., Chuah, C.Y., Kim, J., Kim, Y., Ko, N., Seo, Y., Kim, K., Bae, T.H., and Lee, E. (2018). Separation of Acetylene from Carbon Dioxide and Ethylene by a Water-Stable Microporous Metal–Organic Framework with Aligned Imidazolium Groups inside the Channels. Angew. Chem. Int. Ed. *57*, 7869-7873.

12 Zeng, H., Xie, M., Huang, Y.L., Zhao, Y., Xie, X.J., Bai, J.P., Wan, M.Y., Krishna, R., Lu, W., and Li, D. (2019). Induced Fit of C_2H_2 in a Flexible MOF Through Cooperative Action of Open Metal Sites. Angew. Chem. Int. Ed. *58*, 8515-8519.

13 Zhang, L., Jiang, K., Yang, L., Li, L., Hu, E., Yang, L., Shao, K., Xing, H., Cui, Y., Yang, Y., Li, B., Chen, B., and Qian, G. (2021). Benchmark C_2H_2/CO_2 Separation in an Ultra-Microporous Metal–Organic Framework via Copper(I)-Alkynyl Chemistry. Angew. Chem. Int. Ed. *60*, 15995-16002.

14 Niu, Z., Cui, X., Pham, T., Verma, G., Lan, P.C., Shan, C., Xing, H., Forrest, K.A., Suepaul, S., Space, B., Nafady, A., Al-Enizi, A.M., and Ma, S. (2021). A MOF-based Ultra-Strong Acetylene Nano-trap for Highly Efficient C_2H_2/CO_2 Separation. Angew. Chem. Int. Ed. *60*, 5283-5288.

15 Peng, Y.-L., Pham, T., Li, P., Wang, T., Chen, Y., Chen, K.-J., Forrest, K.A., Space, B., Cheng, P., Zaworotko, M.J., and Zhang, Z. (2018). Robust Ultramicroporous Metal-Organic Frameworks with BenchmarkAffinity forAcetylene. Angew. Chem. Int. Ed. *57*, 10971-10975.

16 Li, P., He, Y., Zhao, Y., Weng, L., Wang, H., Krishna, R., Wu, H., Zhou, W., O'Keeffe, M., Han, Y., and Chen, B. (2015). A Rod-Packing Microporous Hydrogen-Bonded Organic Framework for Highly Selective Separation of C_2H_2/CO_2 at Room Temperature. Angew. Chem. Int. Ed. *54*, 574-577.

17 Scott, H.S., Shivanna, M., Bajpai, A., Madden, D.G., Chen, K.J., Pham, T., Forrest, K.A., Hogan, A., Space, B., Perry Iv, J.J., and Zaworotko, M.J. (2017). Highly Selective Separation of C_2H_2 from CO_2 by a New Dichromate-Based Hybrid Ultramicroporous Material. ACS Appl. Mater. Interfaces *9*, 33395-33400.

18 Luo, F., Yan, C., Dang, L., Krishna, R., Zhou, W., Wu, H., Dong, X., Han, Y., Hu, T.L., O'Keeffe, M., Wang, L., Luo, M., Lin, R.B., and Chen, B. (2016). UTSA-74: A MOF-74 Isomer with Two Accessible Binding Sites per Metal Center for Highly Selective Gas Separation. J. Am. Chem. Soc. *138*, 5678-5684.

19 Chen, K.-J., Scott, H.S., Madden, David G., Pham, T., Kumar, A., Bajpai, A., Lusi, M., Forrest, Katherine A., Space, B., Perry, John J., and Zaworotko, Michael J. (2016). Benchmark C_2H_2/CO_2 and CO_2/C_2H_2 Separation by Two Closely Related Hybrid Ultramicroporous Materials. Chem *1*, 753-765.

20 Ye, Y., Ma, Z., Lin, R.B., Krishna, R., Zhou, W., Lin, Q., Zhang, Z., Xiang, S., and Chen, B. (2019). Pore Space Partition within a Metal-Organic Framework for Highly Efficient C_2H_2/CO_2 Separation. J. Am. Chem. Soc. *141*, 4130-4136.

21 Zeng, H., Xie, M., Huang, Y.-L., Zhao, Y., Xie, X.-J., Bai, J.-P., Wan, M.-Y., Krishna, R., Lu, W., and Li, D. (2019). Induced Fit of C_2H_2 in a Flexible MOF Through Cooperative Action of Open Metal Sites. Angew. Chem. Int. Ed. *58*, 8515-8519.

22 Xiang, S., Zhou, W., Zhang, Z., Green, M.A., Liu, Y., and Chen, B. (2010). Open metal sites within isostructural metal-organic frameworks for differential recognition of acetylene and extraordinarily high acetylene storage capacity at room temperature. Angew. Chem. Int. Ed. *49*, 4615-4618.

23 Chen, C.X., Zheng, S.P., Wei, Z.W., Cao, C.C., Wang, H.P., Wang, D.W., Jiang, J.J., Fenske, D.T., and Su, C.Y. (2017). A Robust Metal-Organic Framework Combining Open Metal Sites and Polar Groups for Methane Purification and CO_2/Fluorocarbon Capture. Chem. Eur. J. *23*, 4060-4064.

24 Yoon, J.H., Choi, S.B., Oh, Y.J., Seo, M.J., Jhon, Y.H., Lee, T.-B., Kim, D., Choi, S.H., and Kim, J. (2007). A porous mixed-valent iron MOF exhibiting the acs net: Synthesis, characterization and sorption behavior of $Fe_3O(F_4BDC)_3(H_2O)_3\cdot(DMF)_{3.5}$. Catal. Today *120*, 324-329.

25 Sheldrick, G. (2008). A short history of SHELX. Acta Crystallogr A *64*, 112-122.

26 Czepirski, J.J.L. (1989). Chem. Eng. Sci. *44*, 797-801.

27 Myers, A.L., and Prausnitz, M. (1965). J. AIChE *11*, 121-127.

28 Material Studios, v.A.S.I., San Diego, CA 92121, USA. (2001–2011.).

29 Jones, J.E. (1924). Proc. R. Soc. A *106*, 463–477.

30 Jorgensen, W.L., Maxwell, D.S., and Tirado-Rives, J. (1996). J. Am. Chem. Soc. *118*, 11225-11236.

31 Rappé, A.K., Casewit, C.J., Colwell, K.S., Goddard, W.A., and Skiff, W.M. (1992). J. Am. Chem. Soc. *114*, 10024–10035.

32 Wilmer, C.E., Kim, K.C., and Snurr, R.Q. (2012). J. Phys. Chem. Lett. *3*, 2506-2511.

33 Kirkpatrick, S., Gelatt, C.D., and Vecchi, M.P. (1983). Science *220*, 671-680.

34 Scott, H.S., Shivanna, M., Bajpai, A., Madden, D.G., Chen, K.-J., Pham, T., Forrest, K.A., Hogan, A., Space, B., Perry IV, J.J., and Zaworotko, M.J. (2017). ACS Appl. Mater. Interfaces *9*, 33395-33400.

35 Franz, D.M., Dyott, Z.E., Forrest, K.A., Hogan, A., Pham, T., and Space, B. (2018). Phys. Chem. Chem. Phys. *20*, 1761-1777.

36 Mullen, A.L., Pham, T., Forrest, K.A., Cioce, C.R., McLaughlin, K., and Space, B.J. (2013). J. Chem. Theory Comput. *9*, 5421-5429.

37 Ewald, P.P. (1921). Ann. Phys. *369*, 253-287.

38 Wells, B.A., and Chaffee, A.L. (2015). J. Chem. Theory Comput. *11*, 3684-3695.

39 Belof, J.L., and Space, B. (2012). Massively Parallel Monte Carlo (MPMC), Available on GitHub. https://github.com/mpmccode/mpmc.

40 Franz, D.M., Belof, J.L., McLaughlin, K., Cioce, C.R., Tudor, B., Hogan, A., Laratelli, L., Mulcair, M., Mostrom, M., Navas, A., Stern, A.C., Forrest, K.A., Pham, T., and Space, B. (2019). Adv. Theory Simul. *2*, 1900113.

41 Frenkel, D., and Smit, B. (2002). Understanding Molecular Simulation: From Algorithms to Applications. Academic Press: New York, 112-114.

42 Cui, X., Chen, K., Xing, H., Yang, Q., Krishna, R., Bao, Z., Wu, H., Zhou, W., Dong, X., Han, Y., Bin Li, Ren, Q., Zaworotko, M.J., and Chen, B. (2016). Pore chemistryandsize control in hybrid porous materials foracetylene capture from ethylene. Science *353*, 141-144.

43 Krishna, R. (2014). The Maxwell-Stefan Description of Mixture Diffusion in Nanoporous Crystalline Materials. Microporous Mesoporous Mater. *185*, 30-50.

44 Krishna, R. (2015). Methodologies for Evaluation of Metal-Organic Frameworks in Separation Applications. RSC Adv. *5*, 52269-52295.

45 Krishna, R. (2017). Screening Metal-Organic Frameworks for Mixture Separations in Fixed-Bed Adsorbers using a Combined Selectivity/Capacity Metric. RSC Adv. *7*, 35724-35737.

46 Krishna, R. (2018). Methodologies for Screening and Selection of Crystalline Microporous Materials in Mixture Separations. Sep. Purif. Technol. *194*, 281-300.

47 Krishna, R. (2020). Metrics for Evaluation and Screening of Metal-Organic Frameworks for Applications in Mixture Separations. ACS Omega *5*, 16987−17004.